1   **eIF2B Conformation and Assembly State Regulate the Integrated Stress Response**

2   Michael Schoof[1,2], Morgane Boone[1,2,#], Lan Wang[1,2,#], Rosalie Lawrence[1,2,#], Adam Frost[2,3,*],

3   Peter Walter[1,2,*]

4

5   **Affiliations**

6   [1]Howard Hughes Medical Institute, University of California at San Francisco, San Francisco, CA,

7   USA.

8   [2]Department of Biochemistry and Biophysics, University of California at San Francisco, San

9   Francisco, CA, USA.

10   [3]Chan Zuckerberg Biohub, San Francisco, CA, USA.

11

12   [#] These authors contributed equally

13   * To whom correspondence should be addressed; Email: Peter@walterlab.ucsf.edu;

14   Adam.frost@ucsf.edu

15

16   Subject Areas: Biochemistry and Chemical Biology, Cell Biology

Abstract

The integrated stress response (ISR) is activated by phosphorylation of the translation initiation factor eIF2 in response to various stress conditions. Phosphorylated eIF2 (eIF2-P) inhibits eIF2's nucleotide exchange factor eIF2B, a two-fold symmetric heterodecamer assembled from subcomplexes. Here, we monitor and manipulate eIF2B assembly *in vitro* and *in vivo.* In the absence of eIF2B's α-subunit, the ISR is induced because unassembled eIF2B tetramer subcomplexes accumulate in cells. Upon addition of the small-molecule ISR inhibitor ISRIB, eIF2B tetramers assemble into active octamers. Surprisingly, ISRIB inhibits the ISR even in the context of fully assembled eIF2B decamers, revealing allosteric communication between the physically distant eIF2, eIF2-P, and ISRIB binding sites. Cryo-EM structures suggest a rocking motion in eIF2B that couples these binding sites. eIF2-P binding converts eIF2B decamers into 'conjoined tetramers' with diminished substrate binding and enzymatic activity. Canonical eIF2-P-driven ISR activation thus arises due to this change in eIF2B's conformational state.

Introduction

All cells must cope with stress, ranging from nutrient deprivation to viral infection to protein misfolding. Cell stress may arise from cell-intrinsic, organismal, or environmental insults, yet often converges on common regulatory nodes. The integrated stress response (ISR) is a conserved eukaryotic stress response that senses and integrates diverse stressors and responds by reprogramming translation (Harding et al. 2003). ISR activation has been linked to numerous human diseases, including cancer and neurological diseases (reviewed in Costa-Mattioli and Walter, 2020). While acute ISR activation largely plays a cytoprotective role, its dysregulation (both aberrant activation and insufficient activation) can negatively affect disease progression. In many pathological conditions, for example, the ISR is constitutively activated and maladaptive effects arise that worsen the disease outcome. Many conditions of cognitive dysfunction, for example, have been linked causally to ISR activation in mouse models, including brain trauma resulting from physical brain injuries (Chou et al. 2017; Sen et al. 2017), familial conditions including Vanishing White Matter Disease and Down syndrome (Leegwater et al. 2001; van der Knaap et al. 2002; Zhu et al. 2019), neurodegenerative diseases such as Alzheimer's and ALS (Atkin et al. 2008; Ma et al. 2013), and even the cognitive decline associated with normal aging (Sharma et al. 2018; Krukowski et al. 2020). Our understanding of the molecular mechanism of ISR regulation therefore is of profound importance.

Translation reprogramming upon ISR induction results as a consequence of reduced ternary complex (TC) levels. The TC is composed of methionyl initiator tRNA (Met-tRNA[i]), the general translation initiation factor eIF2, and GTP (Algire, Maag, and Lorsch 2005). At normal, saturating TC concentrations, translation initiates efficiently on most mRNAs containing AUG translation start sites; however, translation of some mRNAs is inhibited under these conditions by the presence of inhibitory small upstream open reading frames (uORF) in their 5' untranslated regions (Hinnebusch, Ivanov, and Sonenberg 2016). When TC levels are sub-saturating, translation is repressed on most mRNAs. In contrast, some mRNAs that contain uORFs in their 5'UTRs are now preferentially translated, including mRNAs encoding stress-responsive transcription factors, such as ATF4 (Harding et al. 2000). Thus TC availability emerges as a prime factor in determining the translational and, consequentially, the transcriptional programs of the cell.

63   The central mechanism that regulates TC levels in response to stress conditions concerns the

64   loading of eIF2's γ subunit with GTP. Without GTP, eIF2 cannot bind Met-tRNA[i] and hence does

65   not assemble the TC. Loading is catalyzed by the guanine nucleotide exchange factor (GEF)

66   eIF2B, a large decameric and two-fold symmetric enzyme that is composed of two copies each

67   of five different subunits, eIF2Bα, β, δ, γ, and ε (Kashiwagi et al. 2016; Tsai et al. 2018;

68   Wortham et al. 2014; Zyryanova et al. 2018). Stress sensing is accomplished by four upstream

69   kinases (PKR, PERK, GCN2, and HRI) that are activated by different stress conditions and, in

70   turn, phosphorylate eIF2 as a common target (Hinnebusch 2005; Guo et al. 2020; Dey et al.

71   2005; Shi et al. 1998). Phosphorylation by each of these kinases converges on a single amino

72   acid, S51, in eIF2's α subunit (eIF2α). As a profound consequence of eIF2α S51

73   phosphorylation, eIF2 converts from eIF2B's substrate for GTP exchange into a potent eIF2B

74   inhibitor.

75

76   Cryo-EM studies of eIF2B•eIF2 complexes show that eIF2 snakes across the surface of eIF2B

77   in an elongated conformation, contacting eIF2B at four discontinuous interfaces, which we here

78   refer to as IF1 – IF4 (Figure 1 – figure supplement 1) (Kenner et al. 2019; Gordiyenko, Llácer,

79   and Ramakrishnan 2019; Kashiwagi et al. 2019; Adomavicius et al. 2019). IF1 and IF2 engage

80   eIF2γ (containing eIF2's GTPase domain) with eIF2Bε, sandwiching eIF2γ between eIF2Bε's

81   catalytic and core-domain respectively. This interaction pries the GTP binding site open, thus

82   stabilizing the apo-state to catalyze nucleotide exchange. IF3 and IF4 engage eIF2 via its α

83   subunit across eIF2B's two-fold symmetry interface, where two eIF2Bβδγε tetramer

84   subcomplexes are joined. The eIF2α binding surfaces line a cleft between eIF2Bβ (IF3) and

85   eIF2Bδ' (IF4) (the prime to indicate the subunit in the adjoining tetramer). Upon S51

86   phosphorylation, eIF2α adopts a new conformation that renders it incompatible with IF3/IF4

87   binding (Bogorad, Lin, and Marintchev 2017; Kenner et al. 2019; Zhu et al. 2019; Kashiwagi et

88   al. 2019; Adomavicius et al. 2019; Gordiyenko, Llácer, and Ramakrishnan 2019). Rather,

89   phosphorylation unlocks an entirely new binding mode on the opposite side of eIF2B, where

90   eIF2α-P now binds to a site between eIF2Bα and eIF2Bδ. We and others previously proposed

91   that, when bound to eIF2B in this way, the β and especially the γ subunits of eIF2-P could

92   sterically block eIF2γ of a concomitantly bound unphosphorylated eIF2 substrate from engaging

93   productively with eIF2Bε's active site (Kashiwagi et al. 2019; Kenner et al. 2019). Such a

94   blockade could explain the inhibitory effect of eIF2-P, and this model predicts that GEF inhibition

95   should depend on eIF2γ as the entity responsible for causing the proposed steric clash.

96

97   Both eIF2 and eIF2-P binding sites span interfaces between eIF2B subunits present in the

98   decamer but not in the subcomplexes from which it is assembled. The eIF2B decamer is built

99   from two eIF2Bβδγε tetramers and one eIF2Bα$_2$ homodimer (Wortham et al. 2014; Tsai et al.

100   2018). These subcomplexes are stable entities that, when mixed *in vitro,* readily assemble into

101   decamers. The eIF2Bβδγε tetramer has a low, basal GEF activity, as it can only engage with

102   eIF2 through IF1 - IF3 (Tsai et al. 2018; Craddock and Proud 1996). As expected, eIF2B

103   decamer assembly results in a >20-fold rate enhancement of nucleotide exchange, presumably

104   due to enhanced substrate binding caused by the completion of the eIF2α binding site through

105   the addition of IF4 (Tsai et al. 2018; Craddock and Proud 1996). Assembly of the eIF2B

106   decamer is driven by eIF2Bα$_2$, which acts as an assembly promoting factor. Thus, eIF2B

107   assembly into a decamer allows the modalities of i) full GEF activity on eIF2 and ii) inhibition by

108   eIF2-P to manifest.

109

110   The activity of the ISR can be attenuated by ISRIB, a potent small drug-like molecule with

111   dramatic effects (Sidrauski et al. 2013). In mice, ISRIB corrects with no overt toxicity the

112   cognitive deficits caused by traumatic brain injury (Chou et al. 2017), Down syndrome (Zhu et

113   al. 2019), normal aging (Krukowski et al. 2020), and other brain dysfunctions (Wong et al. 2018)

114   with an extraordinary efficacy, indicating that the molecule reverses the detrimental effects of a

115   persistent and maladaptive state of the ISR. ISRIB also kills metastatic prostate cancer cells

116   (Nguyen et al. 2018). ISRIB's mechanistic target is eIF2B to which it binds in a binding groove

117   that centrally bridges the symmetry interface between eIF2Bβδγε tetramers (Sekine et al. 2015;

118   Tsai et al. 2018; Zyryanova et al. 2018; Sidrauski et al. 2015). As such, it acts as a "molecular

119   staple", promoting assembly of two eIF2Bβδγε tetramers into an enzymatically active

120   eIF2B(βδγε)$_2$ octamer. Here, we further interrogated the role of ISRIB by engineering cells that

121   allow us to monitor and experimentally manipulate eIF2B's assembly state. These experiments

122   led to the discovery of a conformational switch that negatively couples the eIF2 and eIF2-P

123   binding sites and the ISRIB binding site by allosteric communication in the eIF2B complex. This

124   conformational switch is the central mechanism by which ISR activation occurs.

125

126   **Results**

127   **eIF2B assembly state modulates the ISR in cells.**

128   To investigate the role of eIF2B's assembly state in controlling ISR activation, we developed

129   ISR reporter cells that enable experimental modulation of the eIF2B decamer concentration. To

130   this end, we tagged eIF2Bα with an FKBP12[F36V] degron in human K562 cells (Figure 1 – figure

131   supplement 2A and B), using CRISPR-Cas9 to edit the endogenous locus. The cell-permeable

132   small molecule dTag13 induces selective degradation of the FKBP12^{F36V}-tagged eIF2Bα (Figure

133   1A) (Nabet et al. 2018). We also engineered a genomically integrated dual ISR reporter system

134   into these cells. The reporter system consists of the mNeonGreen fluorescent protein placed

135   under translational control of a uORF-containing 5' untranslated region (UTR) derived from

136   ATF4 ("ATF4 reporter") and the mScarlet-i fluorescent protein containing a partial ATF4 5' UTR

137   from which the uORFs have been removed ("general translation reporter"). To optimize the

138   signal of these reporters, we fused both fluorescent proteins to the ecDHFR degron (Figure 1 –

139   figure supplement 3). This degron drives the constitutive degradation of the fusion proteins

140   unless the small molecule trimethoprim is added to stabilize them (Iwamoto et al. 2010). In this

141   way, the reporters allow us to monitor only *de novo* translation. Unless otherwise stated,

142   trimethoprim was added concurrently with other treatments.

143

144   Treating ISR reporter cells with the small molecule dTag13 led to rapid and complete

145   degradation of FKBP12^{F36V}-tagged eIF2Bα (Figure 1B). As expected, eIF2Bα degradation was

146   selective, as eIF2Bδ, which binds directly to eIF2Bα in the decamer, remained intact. dTag13

147   treatment also did not increase eIF2α phosphorylation, a hallmark of canonical ISR activation by

148   ISR kinases (Figure 1B). Nevertheless, dTag13-induced eIF2Bα degradation led to increased

149   translation of the ATF4 reporter and decreased translation of the general translation reporter

150   (Figure 1C and Figure 1 – figure supplement 4A) in a concentration-dependent manner. dTag13

151   treatment of cells lacking FKBP12^{F36V} degron-tagged eIF2Bα did not induce the ISR (Figure 1 –

152   figure supplement 5). These results demonstrate that ISR-like translational reprogramming

153   follows eIF2Bα depletion.

154

155   **ISRIB resolves assembly-based stress**.

156   As predicted from previous *in vitro* work, ISRIB entirely reversed the ISR translational

157   reprogramming by eIF2Bα depletion (EC$_{50}$ = 1.4 nM; Figure 1D and Figure 1 – figure

158   supplement 4B) (Tsai et al. 2018). Thus, eIF2Bα can be quantitatively replaced by ISRIB, a

159   small molecule that causes eIF2B(βδγε)$_2$ octamer assembly, rendering the eIF2B decamer and

160   ISRIB-stabilized octamer functional equivalents in these cells. dTag13 treatment led to

161   continued increases in ATF4 translation and decreased general translation over a 6-hour

162   window (Figure 1E, Figure 1 – figure supplement 4C), and co-treatment with ISRIB completely

163   reversed ISR activation.

164

By contrast, ISRIB inhibited eIF2-P-based stress induced by thapsigargin treatment only at early time points (1-3 hours), whereas at later time points, ISRIB showed greatly diminished effects in blocking ISR activation. These data distinguish eIF2B assembly-based stress and eIF2-P-based stress in their response to mitigation by ISRIB.

FRET reporters monitor eIF2B assembly state.

To directly measure eIF2B's assembly state, we tagged eIF2B subunits with fluorescent protein pairs and used Förster resonance energy transfer (FRET) as a readout of their molecular proximity. We tagged the C-terminus of eIF2Bβ with mNeonGreen as the FRET donor and the C-terminus of eIF2Bδ with mScarlet-i as the FRET acceptor. In this arrangement, donor and acceptor proteins would be in the range of 120-140 Å apart in the eIF2Bβδγε tetramer (expected negligible FRET efficiency) and become juxtaposed at a distance closer to 60-80 Å when two eIF2B tetramers assemble into an octamer or a decamer (expected moderate FRET efficiency). Therefore, this genetically encodable system promised to provide us with a quantitative assay of eIF2B's assembly state.

To first characterize these tools *in vitro*, we co-expressed the fluorescently tagged eIF2Bβ and eIF2Bδ fusion proteins together with untagged eIF2Bγ and eIF2Bε in *E. coli* and purified the tetramer as previously described (Tsai et al. 2018). Analysis by analytical ultracentrifugation following absorbance at 280 nm demonstrated that the fluorescent protein tags do not interfere with tetramer stability (Figure 2 – figure supplement 1). Moreover, consistent with our previous work, addition of separately expressed eIF2Bα homodimers (eIF2Bα$_2$) readily assembled fluorescently-tagged eIF2Bβδγε tetramers (eIF2Bβδγε-F) into complete eIF2B decamers. Similarly, the addition of ISRIB caused the tagged tetramers to assemble into octamers.

Upon donor excitation at 470 nm, we next monitored the ratio of fluorescence at 516 nm (donor peak) and 592 nm (acceptor peak) as a function of eIF2Bα$_2$ and ISRIB concentrations. The results validated our system: in both cases, the FRET signal reliably reported on eIF2Bβδγε-F tetramer assembly into the respective larger complexes with half-maximal assembly (EC$_{50}$) at 250 nM of ISRIB and 20 nM of eIF2Bα$_2$ (Figure 2B and C). Kinetic analysis showed that eIF2Bα$_2$ drives assembly of eIF2Bβδγε-F tetramers into decamers with a t$_{1/2}$ of 7 min and that ISRIB drives eIF2Bβδγε-F tetramers into octamers with similar kinetics (t$_{1/2}$ = 5 min) (Figure 2D and E; 0-55 min time window). By contrast, the dissociation kinetics of eIF2Bα$_2$-stabilized decamers and ISRIB-stabilized octamers differed substantially. Spiking in an excess of

199   unlabeled eIF2Bβδγε tetramers to trap dissociated eIF2Bβδγε-F tetramers into dark complexes

200   revealed slow eIF2Bα$_2$-stabilized decamer dissociation kinetics ($t_{1/2}$ = 3 h), whereas ISRIB-

201   stabilized octamers dissociated much faster ($t_{1/2}$ = 15 min) (Figure 2D and E; 55-150 min time

202   window).

203

204   Still *in vitro*, as expected, co-treatment of ISRIB and eIF2Bα$_2$ did not induce greater complex

205   assembly when eIF2Bα$_2$ was at saturating concentrations (Figure 2F). However, ISRIB

206   substantially enhanced complex stability, slowing the dissociation rate of the ISRIB-stabilized

207   decamer such that no discernible dissociation was observed. Critically, pre-addition of excess

208   untagged eIF2Bβδγε and tetramer dimerizers (either eIF2Bα$_2$ or ISRIB) led to no change in

209   FRET signal above baseline (Figure 2 – figure supplement 2A, B, and C). This observation

210   confirms that the lack of signal loss in the ISRIB-stabilized decamer is indeed due to increased

211   complex stability and not to sequestering of dimerizer by the untagged tetramer. Consistent with

212   these observations, treatment with ISRIB at saturating eIF2Bα$_2$ concentrations did not lead to a

213   further increase in eIF2B's nucleotide exchange activity as monitored by BODIPY-FL-GDP

214   nucleotide exchange (Figure 2 – figure supplement 3).

215

216   **eIF2B exists as a decamer in K562 cells.**

217   Turning to live cells to monitor and modulate the assembly state of eIF2B, we engineered K562

218   cells to contain both the FRET reporters (eIF2Bβ-mNeonGreen-FLAG and eIF2Bδ-mScarlet-i-

219   myc) and eIF2Bα-FKBP12^{F36V} (Figure 1 – figure supplement 2A and B). Consistent with our

220   data on the ISR reporter in Figure 1, degradation of eIF2Bα led to translation of ATF4, whereas

221   eIF2α-P and eIF2Bδ levels remain unchanged (Figure 3A).

222

223   Importantly, degradation of eIF2Bα via dTag13 treatment led to eIF2B complex disassembly, as

224   monitored by FRET signal (Figure 3B), validating that our FRET system robustly reports on the

225   eIF2B complex assembly state in living cells. At the 3-hour time point, the EC$_{50}$ for eIF2B

226   disassembly was 5 nM (Figure 3B), which mirrors the EC$_{50}$ for ISR activation (15 nM, Figure

227   1B). These data indicate that eIF2B's assembly state is intimately linked to translational output.

228

229   **ISRIB inhibits the ISR without impacting eIF2B's assembly state.**

230   We next treated cells with a titration of ISRIB +/- the addition of optimal dTag13 concentration

231   (83 nM, plateau from Figure 1B and 3B) for 3 hours (Figure 3C). ISRIB assembled tetramers

232   into octamers when the eIF2Bα subunit was not present. Notably, in the presence of eIF2Bα,

233 the FRET signal remained unchanged upon increasing ISRIB concentrations, indicating that the

234 assembly state of eIF2B in K562 cells is largely decameric unless eIF2Bα is compromised.

235

236 As ISRIB's effect on translation is only noticeable upon cellular stress, we wondered whether

237 the assembly state of eIF2B could be affected by stress. To this end, we treated cells with

238 thapsigargin +/- ISRIB. We observed no decrease in FRET signal upon ER stress or ISRIB

239 treatment, arguing that eIF2B exists as a fully assembled decamer in both stressed and

240 unstressed cells (Figure 3D).

241

242 Nevertheless, ISRIB resolved both eIF2-P-based activation of the ISR induced by thapsigargin

243 and assembly-based activation of the ISR induced by eIF2Bα depletion (Figure 3E, lanes 4 and

244 6), implying that while ISRIB does not alter eIF2B's assembly state in the thapsigargin-treated

245 cells, it still impacts ISR signaling. Thus ISRIB must somehow overcome the inhibition of

246 eIF2B's GEF activity asserted by eIF2-P binding.

247

248 **ISRIB blocks eIF2-P binding to eIF2B.**

249 To resolve this paradox, we immunoprecipitated eIF2B complexes, pulling on eIF2Bβ-

250 mNeonGreen-FLAG, to assess whether eIF2-P binding changes upon ISRIB treatment in

251 thapsigargin-stressed cells (Figure 4A). Consistent with canonical ISR activation, in total cell

252 lysate eIF2α-P levels increased upon stress to a similar extent with and without ISRIB

253 treatment. At the same time, ATF4 translation occurred in stressed cells only, and ISRIB

254 treatment inhibited ATF4 translation (Figure 4A, lanes 1-3).

255

256 Surprisingly, we found that the amount of eIF2α-P bound to eIF2B was dramatically reduced in

257 the immunoprecipitations from ISRIB-treated cells (Figure 4A, lanes 4-6). Because the amount

258 of total eIF2α bound by eIF2B is likewise reduced, this result suggests that under these stress

259 conditions the majority of eIF2B-bound eIF2 still associated after immunoprecipitation is

260 phosphorylated (note that the eIF2 antibody used in this analysis detects both eIF2α and eIF2α-

261 P). Thus, ISRIB antagonizes eIF2-P binding to eIF2B. Because the binding sites for ISRIB and

262 eIF2-P are ~50 Å apart, this result suggests an allosteric rather than an orthosteric interplay

263 between ISRIB and eIF2-P binding.

264

265 **eIF2α-P is sufficient to impair ISRIB binding to eIF2B.**

266 To test this notion, we next examined whether, reciprocally, eIF2-P inhibits ISRIB binding *in*
267 *vitro*. To this end, we used a fluorescent ISRIB analog (FAM-ISRIB) that emits light with a higher
268 degree of polarization when bound to eIF2B compared to being free in solution (Zyryanova et al.
269 2018). As previously shown, ISRIB competed with FAM-ISRIB for eIF2B binding (Figure 4B)
270 (Zyryanova et al. 2018). Indeed, our results show that eIF2-P, but not eIF2, competes with FAM-
271 ISRIB binding (Figure 4C). In fact, eIF2α-P, that is, eIF2's phosphorylated α-subunit alone, but
272 not eIF2α, its unphosphorylated form, suffices in this assay (Figure 4D). This observation
273 defines eIF2α-P as the minimal unit needed to affect ISRIB release.
274
275 We confirmed this model with assays that used the eIF2 kinase PKR to phosphorylate eIF2α,
276 thereby over time converting this previously inert component into eIF2α-P, the ISRIB-binding
277 antagonist (Figure 4E). Conversely, dephosphorylation of eIF2α-P by λ phosphatase over time
278 destroyed its ability to dislodge FAM-ISRIB (Figure 4F). Together, these data show that ISRIB
279 binding and eIF2α-P or eIF2-P binding are mutually exclusive events.
280
281 **eIF2α-P is sufficient to inhibit eIF2B GEF activity.**
282 We further extend these conclusions with activity-based assays. As previously shown, in
283 nucleotide exchange assays that monitor eIF2B's GEF activity towards eIF2, eIF2-P inhibited
284 eIF2B GEF activity in a concentration-dependent manner (Figure 5A) (Wong et al. 2018). ISRIB
285 partially rescued the activity (Figure 5C). Remarkably, the phosphorylated α subunit alone
286 (eIF2α-P) inhibited eIF2B GEF activity (Figure 5B), and ISRIB again partially rescued activity
287 (Figure 5D). This observation is inconsistent with previous models that emphasized the potential
288 for a steric clash between the γ subunit of eIF2-P and the γ subunit of the substrate eIF2
289 (Kenner et al. 2019; Kashiwagi et al. 2019). Therefore these data support the notion that the
290 phosphorylated α subunit of eIF2 alone suffices to modulate eIF2B activity, i.e., that orthosteric
291 competition cannot wholly explain eIF2-P's inhibitory properties and that the remaining eIF2
292 subunits are dispensable for this effect.
293
294 **eIF2α-P decreases eIF2B's enzymatic activity and antagonizes eIF2 binding.**
295 To explain how eIF2α-P alone could block GEF activity, we considered three principle options: i)
296 eIF2α-P may decrease the rate of eIF2B's enzymatic activity, ii) it may allosterically inhibit eIF2
297 binding to eIF2B, or iii) it may perform some combination of those mechanisms. To investigate
298 the relative contributions of these mechanisms, we employed multiple turnover kinetic
299 measurements of eIF2B activity at varying eIF2 concentrations. We measured the initial velocity

300   of this reaction and performed Michaelis Menten analysis to determine the V_{max} and the K_M of

301   the GEF reaction at varying concentrations of eIF2α-P (Figure 6A and Figure 6 – figure

302   supplement 1). Notably, with increasing concentrations of eIF2α-P, the V_{max} decreased while K_M

303   increased, suggesting that both substrate affinity and eIF2B catalytic activity were affected by

304   eIF2α-P binding. We next examined how inhibited eIF2B decamers compared to tetramers.

305   Intriguingly, at near-saturating eIF2α-P concentrations, the k_{cat} / K_M ratio, a measure of specific

306   enzyme activity, approached that of the eIF2Bβδγε tetramer, suggesting that eIF2α-P inhibits

307   the decamer by converting it to a tetramer-like state, rendering eIF2α-P-inhibited eIF2B

308   decamers and eIF2B tetramers functionally equivalent (Figure 6B and Figure 6 – figure

309   supplement 1).

310

311   To further examine whether eIF2 and eIF2α-P antagonize one another's binding, we

312   immobilized eIF2B decamers on agarose beads and incubated with combinations of eIF2,

313   eIF2α-P, and ISRIB (Figure 6C). eIF2 readily bound to eIF2B with and without ISRIB (lanes 1

314   and 2) but eIF2α-P addition reduced the amount of eIF2 recovered (lane 3). As expected, ISRIB

315   inhibited eIF2α-P binding and restored normal eIF2 binding (lane 4). Additionally, we utilized

316   FAM-ISRIB as a tool to read out the eIF2-bound active state of eIF2B. Consistent with the data

317   shown in Figures 4E and 4F, eIF2B addition to FAM-ISRIB increased polarization (Figure 6D,

318   black and red data points, respectively), and FAM-ISRIB binding was blocked by the addition of

319   eIF2α-P (blue data point on the y-axis). A titration of eIF2 into this reaction allowed FAM-ISRIB

320   polarization to recover, indicating that eIF2 binds and disrupts eIF2α-P's inhibitory binding,

321   which restores FAM-ISRIB binding. This result reinforces the notion that eIF2 and ISRIB binding

322   are synergistic, i.e., positively coupled.

323

324   **eIF2α-P inhibits eIF2B by inducing a conformational change.**

325   We next turned to structural studies to determine the basis of the decreased enzymatic activity

326   and the apparent antagonism between eIF2α-P and both ISRIB and eIF2. First, we asked

327   whether ISRIB binding alone causes a conformational change in decameric eIF2B. To this end,

328   we prepared the apo-eIF2B decamer by combining eIF2Bβδγε tetramers and eIF2Bα$_2$ and

329   subjected the sample to cryo-EM imaging. After 2D and 3D classification, we generated a single

330   consensus structure of the apo-eIF2B decamer at 2.8 Å resolution (Table 1, Figure 7 – figure

331   supplement 1) with most side chains clearly resolved. This map allowed us to build an improved

332   atomic model of the eIF2B decamer. This structure revealed that apo-eIF2B has an overall very

333   similar structure as the ISRIB-bound decamer published previously (PDB ID: 6CAJ) (Tsai et al.

334   2018; Zyryanova et al. 2018). Closer inspection revealed that ISRIB slightly draws the

335   decamer's two halves together by comparison with the apo state but does not induce marked

336   changes in eIF2B's overall conformation (Figure 7 – figure supplement 2A).

337

338   We next examined the ISRIB-binding pocket. In the apo versus the ISRIB-bound state, eIF2Bδ

339   L179 shifts slightly into the pocket, occupying a position where it would clash with ISRIB

340   binding, and eIF2Bβ H188 (a key ISRIB interactor) adopts a different rotamer (Figure 7 – figure

341   supplement 2B) (Tsai et al. 2018). Overall, however, we conclude that ISRIB binding to the

342   eIF2B decamer correlates with slight rearrangements that are primarily confined to the ISRIB

343   binding pocket. Overlay of the apo decamer with structures of eIF2B bound to one or two copies

344   of its enzymatically-engaged substrate eIF2 also revealed unremarkable changes (Kashiwagi et

345   al. 2019; Kenner et al. 2019; Gordiyenko, Llácer, and Ramakrishnan 2019; Adomavicius et al.

346   2019). We infer from these results that all of these structures represent, with the minor

347   variations noted, the enzymatically active state of eIF2B, henceforth referred to as the "A-State"

348   ("A" for active).

349

350   By contrast, overlaying the eIF2B-eIF2α-P structure (PDB ID: 6O9Z) with the A-State structures

351   revealed significant changes in the overall architecture of eIF2B (Figure 7A), henceforth referred

352   to as the "I-State" ("I" for inhibited) (Kenner et al. 2019). In the I-State, the two symmetrically

353   opposed eIF2B tetramers have undergone a rocking motion that changes the angle between

354   them by 7.5 degrees (Figure 7A). The ISRIB pocket, consequentially, is lengthened by ~2 Å

355   (Figure 7B). Critically, the substrate-binding cleft between eIF2Bβ and eIF2Bδ', where the N-

356   terminal domain of the unphosphorylated eIF2α substrate binds, is widened by 2.6 Å, pulling IF4

357   away but leaving IF1 - IF3 as available binding surfaces (Figure 7C, Figure 7 – figure

358   supplement 3). For both ISRIB and eIF2, these rearrangements break key anchoring

359   interactions, providing a structural explanation why eIF2-P binding destabilizes ISRIB binding

360   and compromises GEF activity. With only 3 of 4 interfaces available, eIF2 can still bind but

361   would bind with lower affinity and may not necessarily be properly positioned, further explaining

362   the reduced catalytic activity observed in Figure 6A. Conversely, in the A-State the cleft

363   between eIF2Bα and eIF2Bδ' is widened by 5.5 Å (Figure 7D), disrupting the eIF2-P binding site

364   and suggesting a possible mechanism for the antagonism between eIF2-P and eIF2/ISRIB.

365

366   Based on these structural comparisons, we conclude that eIF2B adopts at least two notably

367   distinct conformational states, the A- and I-States. These two states are mutually exclusive

368   (Figure 8). The A- and I-States, therefore, define an on-off switch of eIF2B's GEF activity and

369   can be thought of as functional equivalents to the decamer and tetramer assembly states,

370   respectively. The A- to I-State transition thus appears to be the central mechanism underlying

371   ISR activation.

Discussion

As dysregulation of the ISR is increasingly implicated in numerous diseases with devastating consequences, understanding the mechanism of ISR signaling is of profound importance (Costa-Mattioli and Walter 2020). The central ISR regulatory hub is the decameric guanine nucleotide exchange complex eIF2B, which activates eIF2 by loading it with GTP. Upon ISR activation in response to a variety of stress conditions, eIF2 becomes phosphorylated, converting it from eIF2B's substrate into an eIF2B inhibitor. Both eIF2 and eIF2-P are elongated protein complexes that contact eIF2B through multi-subunit, composite interaction surfaces (Kenner et al. 2019; Kashiwagi et al. 2019). The binding mode appears to be determined mainly by eIF2's α subunit, which anchors eIF2 and eIF2-P to their respective binding sites. For the substrate eIF2, binding aligns eIF2γ with eIF2B's catalytic site via IF1 and IF2 for nucleotide exchange. By contrast, for the inhibitor eIF2-P, binding positions its γ-subunit such that it could orthosterically prevent nonphosphorylated eIF2 substrate from engaging the catalytic machinery in eIF2Bε (Kashiwagi et al. 2019; Kenner et al. 2019). While this model was appealing based on the cryo-EM structures of eIF2B•eIF2-P complexes (Kashiwagi et al. 2019), the eIF2α C-terminal domain may retain sufficient flexibility to allow eIF2γ to avert the proposed clash (Adomavicius et al. 2019; Ito, Marintchev, and Wagner 2004).

Expanding from this notion, in this work we show that allosteric rather than clash-based orthosteric competition contributes significantly to eIF2-P-mediated inhibition. We show that eIF2 and eIF2-P binding are negatively coupled, even when only the α subunit of eIF2-P is present. Thus, eIF2α-P binding impairs substrate binding even though the two binding sites are ~50 Å apart. Further, the phosphorylated form of eIF2's α subunit alone inhibits GEF activity both through reduced substrate affinity and reduced eIF2B catalytic efficiency. Indeed, depending on the concentration regime, this change in eIF2B's intrinsic catalytic activity may be the main driver of lowered TC levels. With these data, we demonstrate that the eIF2γ subunit, which would be required for eIF2 inhibition via the clash-based orthosteric model, is mechanistically dispensable for eIF2-P's inhibitory role, although the added binding energy it contributes is certainly of importance in a cellular context.

Cryo-EM reconstructions support this model. They reveal a rocking motion of the two eIF2Bβδγε tetramers with eIF2Bα$_2$ acting as the fulcrum of the movement, akin to a butterfly raising and lowering its wings. These changes are induced by eIF2α-P alone. In the active or "wings-up" A-State, eIF2Bβ and eIF2Bδ' subunits are sufficiently close to fully shape the eIF2α binding site,

14

thus allowing nonphosphorylated substrate engagement. The A-State also contains a properly sized ISRIB binding pocket, thus rendering eIF2 and ISRIB binding synergistic. In contrast, the eIF2α-P binding site is misshapen and lacking properly positioned sidechains critical for eIF2α-P binding. In the inhibited wings-down I-State, the eIF2α-P binding site is shaped correctly, while both the eIF2α (specifically IF4) and ISRIB binding sites are disrupted.

Prior to this work, models describing the molecular function of the drug-like small molecule ISRIB were exclusively focused on ISRIB's activity to promote eIF2B complex assembly. *In vitro* work from our and other labs demonstrated that eIF2Bβδγε tetramers assemble in the presence of ISRIB into eIF2B(βδγε)$_2$ octamers that approach the enzymatic activity of the eIF2B decamer, explaining how ISRIB could promote eIF2B assembly to restock the pool of active eIF2B when depleted by eIF2-P during ISR activation (Tsai et al. 2018; Zyryanova et al. 2018; Sekine et al. 2015; Sidrauski et al. 2015). However, because eIF2Bα$_2$ likewise has assembly-promoting activity, ISRIB can only exert this function when eIF2Bα$_2$ is limiting. We here validated this conjecture in living cells. Experimental depletion of eIF2Bα turned on ISR signaling in the absence of eIF2 phosphorylation, and ISRIB functionally substitutes for eIF2Bα$_2$. In the context of saturating eIF2Bα$_2$ we were thus left with a paradox regarding ISRIB's mechanism of action which we resolve by showing that beyond a role in eIF2B assembly, ISRIB antagonizes eIF2-P binding.

Previous work investigating the effects of compromising eIF2Bα (deletion, mutation, knockdown) did not report on eIF2B complex assembly and were predominantly performed in non-human model systems (Pavitt, Yang, and Hinnebusch 1997; Hannig and Hinnebusch 1988; Elsby et al. 2011). Indeed, it is conceivable that eIF2B subcomplexes (and the role for these complexes in full heterodecamer assembly) are distinct between species. For example, in the fungus *Chaetomium thermophilum,* eIF2Bβ and eIF2Bδ appear to form heterotetrameric subcomplexes (Kuhle, Eulig, and Ficner 2015), whereas we see no evidence for such stable assemblies in our work with human eIF2B. Thus, in other organisms enzymatically active octamers may form, and eIF2Bα's role may thus be primarily to allow eIF2-P binding. Another intriguing possibility is that long-term, cells may enact mechanisms to compensate for the drop in TC levels that accompanies eIF2Bα depletion, consequent decamer disassembly, and decreased eIF2B GEF activity.

439   While our data clearly show that eIF2B is predominantly a decamer in K562 cells, this leaves

440   open the possibility that the assembly state differs by cell type and/or is regulated

441   physiologically. In principle, eIF2Bα could become limiting by regulation of its biosynthesis or

442   degradation, by post-translational modification, and/or by sequestration into an unavailable pool.

443   It is also important to note that an ISRIB-stabilized eIF2B$(\beta\delta\gamma\epsilon)_2$ octamer is inert to inhibition by

444   eIF2-P. Such inhibition would require eIF2α-P to bind at the eIF2Bα/eIF2Bδ interface, which

445   does not exist in complexes lacking eIF2Bα. We speculate that endogenous eIF2B$(\beta\delta\gamma\epsilon)_2$

446   octamers could be stabilized by putative alternate assembly factors, which could be metabolites

447   or proteins that, like ISRIB, can substitute for eIF2Bα_2 in this regard.

448

449   In the course of this study, the demonstration that ISRIB still has a profound effect even in the

450   context of fully assembled eIF2B led to the discovery of allosteric eIF2B regulation. While this

451   manuscript was in preparation, a paper from Takuhiro Ito's and David Ron's laboratories was

452   published that reached similar conclusions regarding ISRIB's effect on allosteric eIF2B

453   regulation (Zyryanova et al. 2021). The work from these groups focuses almost exclusively on

454   the allosteric effects promoted by the drug. Our results agree with their conclusions and

455   demonstrate physiological significance. We show that substrate (eIF2) and inhibitor (eIF2-P)

456   binding are negatively coupled. We additionally show that inhibitor binding reduces eIF2B's

457   catalytic activity. Moreover, we show that by binding to the same binding site on eIF2B, ISRIB

458   can affect the ISR in two modalities: i) by promoting eIF2B assembly under conditions where

459   eIF2Bα_2 is limiting or decamer stability may be compromised, and ii) by biasing allosterically the

460   conformational equilibrium of fully assembled decameric eIF2B towards the A-State, rendering

461   inhibition by eIF2-P more difficult. Conceptually, these two modalities of ISRIB function are quite

462   similar. In both cases, ISRIB promotes the completion of the eIF2α binding site by properly

463   positioning IF4, so that it can cooperate with IF3 to anchor eIF2α. Indeed, in the I-State, the

464   widening of the cleft between eIF2Bβ and eF2Bδ' effectively renders the available interaction

465   surfaces on eIF2B equivalent to those on eIF2B$\beta\delta\gamma\epsilon$ tetramers, limiting eIF2 engagement to IF1-

466   IF3 as IF4 is pulled "out of reach" as it would be in fully dissociated tetramers. In this way, we

467   can think of eIF2B's I-State as "conjoined tetramers" that remain tethered by eIF2Bα_2 but are

468   functionally separate entities.

469

470   Considering the potential pharmacological applications of ISRIB, the relevant modality of ISRIB

471   function may vary between different disease pathologies. In the case of Vanishing White Matter

472   Disease, for example, point mutations destabilize the eIF2B complex and ISRIB therefore may

473   provide primarily a stabilizing effect to recover eIF2B function (Wong et al. 2018). By contrast, in

474   traumatic brain injury, sustained cognitive dysfunction is caused by persistent canonical ISR

475   activation through eIF2-P (Chou et al. 2017). Hence ISRIB would primarily counteract the

476   aberrant ISR activation by predisposing eIF2B to the A-State. Other diseases are likely

477   somewhere along the spectrum of purely assembly-based vs. purely eIF2-P-based ISR

478   activation. Our illustration of the differences between ISRIB's ability to resolve assembly-based

479   stress vs. eIF2-P-based stress should therefore inform how these different diseases are studied

480   and ultimately treated.

481

482   The discovery of allosteric control of eIF2B activity raises intriguing possibilities. Indeed, we can

483   envision that cell-endogenous modulators exist that work as activators (stabilizing the A-State)

484   or inhibitors (stabilizing the I-State). Such putative ISR modulators could be small molecule

485   metabolites or proteins and either bind to the ISRIB binding pocket or elsewhere on eIF2B to

486   adjust the gain of ISR signaling to the physiological needs of the cell. Precedent for this notion

487   comes from viruses that evolved proteins to counteract ISR mediated antiviral defenses. The

488   AcP10 protein in the Bw-CoV SW1 virus, for example, interacts with eIF2B to exert an ISRIB-

489   like effect, likely predisposing eIF2B to the A-state (Rabouw et al. 2020). Regarding the

490   observed changes in the ISRIB binding pocket, the newly gained structural insights can be

491   applied to engineer novel pharmacological ISR modulators that may be effective in opening new

492   therapeutic opportunities in different diseases.

493

494

495

496

497

498   **Materials and Methods**

499   **Cloning of tagged human eIF2B expression plasmids**

500   *eIF2B2* (encoding eIF2Bβ) and *eIF2B4* (encoding eIF2Bδ) had previously been inserted into

501   sites 1 and 2 of pACYCDuet-1, respectively (pJT073) (Tsai et al. 2018). In-Fusion HD cloning

502   (Takarabio) was used to edit this plasmid further and insert mNeonGreen and a $(GS)_5$ linker at

503   the C-terminus of *eIF2B2* and mScarlet-i and a $(GS)_5$ linker at the C-terminus of *eIF2B4*

504   (pMS029). *eIF2B1* (encoding eIF2Bα) had previously been inserted into site 1 of pETDuet-1

505   (pJT075) (Tsai et al. 2018). In-Fusion HD cloning was used to edit this plasmid further and

506   insert a protein C tag (EDQVDPRLIDGK) at the N-terminus of *eIF2B1*, immediately following the

507   pre-existing 6x-His tag (pMS027).

508

509   **Cloning of ATF4 and general translation reporter plasmids**

510   The ATF4 translation reporter was generated using In-Fusion HD cloning. A gBlock containing

511   the ATF4 UTR with both uORF1 and uORF2, ecDHFR, and mNeonGreen was inserted into the

512   pHR vector backbone. The vector was additionally modified to contain a bGH poly(A) signal.

513   The general translation reporter was similarly generated using a gBlock containing a modified

514   ATF4 UTR with both uORF1 and uORF2 removed, ecDHFR, and mScarlet-i.

515

516   **Cloning of eIF2B homology-directed recombination (HDR) template plasmids**

517   HDR template plasmids were generated using Gibson Assembly (NEB) cloning. gBlocks

518   containing mNeonGreen and flanking *eIF2B2* homology arms (pMS074), mScarlet-i and flanking

519   *eIF2B4* homology arms (pMS075), and FKBP12^{F36V} and flanking *eIF2B1* homology arms

520   (pMS101) were inserted into the pUC19 vector. Homology arms were 300bp in all instances.

521

522   **ISR reporter cell line generation**

523   K562 cells expressing dCas9-KRAB as previously generated were used as the parental line

524   (Gilbert et al. 2014). In the ISR reporter cell line, the general translation reporter and the ATF4

525   reporter were integrated sequentially using a lentiviral vector. Vesicular stomatitis virus (VSV)-G

526   pseudotyped lentivirus was prepared using standard protocols and 293METR packaging cells.

527   Viral supernatants were filtered through a 0.45 µm (low protein binding) filter unit (EMD

528   Millipore). The filtered retroviral supernatant was then concentrated 20-fold using an Amicon

529   Ultra-15 concentrator (EMD Millipore) with a 100,000-dalton molecular mass cutoff.

530   Concentrated supernatant was then used the same day or frozen for future use. For spinfection,

531   approximately 900,000 K562 cells were mixed with concentrated lentivirus + virus collection

532   media (DMEM containing 4.5 g/l glucose supplemented with 10% FBS, 6 mM L-glutamine, 15

533   mM HEPES and penicillin/streptomycin), supplemented with polybrene to 8 µg/ml, brought to

534   1.5 mL in a 6-well plate, and centrifuged for 1.5 h at 1000 g. Cells were then allowed to recover

535   and expand for ~1 week before sorting on a Sony SH800 cytometer to isolate cells that had

536   integrated the reporter. Before sorting, cells were treated with 20 µM trimethoprim for 3 h to

537   stabilize the general translation reporter product (ecDHFR-mScarlet-i). mScarlet-i positive cells

538   (targeting a narrow window around median reporter fluorescence) were then sorted into a final

539   pooled population.

540

541 Integration of the ATF4 reporter was performed as above, using the general translation reporter-

542 containing cells as stock for spinfection. At the sorting stage, cells were again treated with 20

543 µM trimethoprim as well as 100 nM thapsigargin (tg) to allow ATF4 reporter translation to be

544 monitored. The highest 3% of mNeonGreen-positive cells were sorted into a final pooled

545 population.

546

547 The *eIF2B1* locus was endogenously edited using modifications to previous protocols (Leonetti

548 et al. 2016). In brief, an HDR template was prepared by PCR amplifying from pMS101 using

549 oligos oMS266 and oMS267 (Table 4). This product was then purified and concentrated to >1

550 µM using magnetic SPRI beads (Beckman Coulter). 2.2 µl Cas9 buffer (580 mM KCl, 40 mM

551 Tris pH 7.5, 2 mM TCEP (tris(20carboxyethyl)phosphine)-HCl, 2 mM $MgCl_2$, and 20% v/v

552 glycerol) was added to 1.3 µl of 100 µM sgRNA (sgMS006, purchased from Synthego) and 2.9

553 µl H_2O and incubated at 70 °C for 5 minutes. 1.6 µl of 62.5 µM Alt-R S.p Cas9 Nuclease V3

554 (IDT) was slowly added to the mix and incubated at 37 °C for 10 min. The donor template was

555 then added to a final concentration of 0.5 µM, and final volume of 10 µl and the RNP mix was

556 stored on ice.

557

558 ISR reporter cells were treated with 200 ng / mL nocodazole (Sigma Aldrich) to synchronize at

559 G2 / M phase for 18 h. Approximately 200,000 cells were resuspended in a mixture of room

560 temperature Amaxa solution (16.4 µl SF Solution, 3.6 µl Supplement (Lonza)). The cell / Amaxa

561 solution mixture was added to the RNP mix and then pipetted into the bottom of a 96-well

562 nucleofection plate (Lonza). This sample was then nucleofected using the 4D-Nucleofector Core

563 unit and 96-well shuttle device (Lonza) with program FF-120. The cells were then returned to

564 pre-warmed RPMI media in a 37 °C incubator and allowed to recover/expand for >1 week.

565 Limiting dilutions of cells were then prepared and plated in individual wells of a 96-well plate and

566 allowed to grow up to identify clonal cells. Identification of edited clones was performed by

567 Western blotting for eIF2Bα and PCR amplification of the edited locus.

568

569 **FRET assembly state reporter cell line generation**

570 eIF2Bβ-mNeonGreen-Flag-tagged cells were generated as described above with pMS074 used

571 to PCR amplify the HDR template and sgMS001 used as the sgRNA. After recovery and

572 expansion, the edited cells were sorted on a Sony SH800 cytometer, and the top 0.1% of

573 mNeonGreen fluorescing cells were sorted into a polyclonal population. After expansion,

574 recovery, and determining that the editing efficiency was over 90% in this population, the
575 polyclonal cells were subjected to a second round of nucleofection using an HDR template
576 amplified off of pMS075 to endogenously tag eIF2Bδ. sgMS004 was used to target the *eIF2B2*
577 locus. Nucleofection conditions were as described above. After ~1 week of recovery and
578 expansion, cells were again sorted as described above to isolate the highest mScarlet-i
579 fluorescing cells. After ~1 week of recovery, limiting dilutions were prepared as described above
580 to isolate and validate editing in individual clones. A fully *eIF2B2*-edited and *eIF2B4*-edited clone
581 was then subjected to a third round of nucleofection to introduce the eIF2Bα-FKBP12^{F36V} fusion.
582 This was performed under identical conditions to those described above for the ISR reporter cell
583 line.
584
585 **ATF4 / general translation reporter assays**
586 ISR reporter cells (at ~500,000 / ml) were co-treated with varying combinations of drugs
587 (trimethoprim, dTag13, thapsigargin, ISRIB) and incubated at 37 °C until the appropriate
588 timepoint had been reached. At this time, the plate was removed from the incubator and
589 samples were incubated on ice for 10 min. Then ATF4 (mNeonGreen) and General Translation
590 (mScarlet-i) reporter levels were read out using a high throughput sampler (HTS) attached to a
591 BD FACSCelesta cytometer. Data was analyzed in FlowJo version 10.6.1, and median
592 fluorescence values for both reporters were exported and plotted in GraphPad Prism 8. Where
593 appropriate curves were fit to log[inhibitor] versus response function with variable slope.
594
595 *In vivo* **FRET assembly state reporter assays**
596 FRET assembly state reporter cells (at ~500,000 / ml) were dosed with varying combinations of
597 drugs (dTag13, thapsigargin, ISRIB) and incubated at 37 °C until the appropriate timepoint had
598 been reached. At this time, the plate was removed from the incubator, and samples were
599 transferred to 5 ml FACS tubes. Samples were kept on ice. FRET signal was measured on a BD
600 FACSAria Fusion cytometer. Data were analyzed in FlowJo version 10.6.1 and median
601 fluorescence values for both mNeonGreen and mScarlet-i emission after mNeonGreen
602 excitation were calculated. The ratio of these two values (termed "FRET signal") was plotted in
603 GraphPad Prism 8. Where appropriate curves were fit to log[inhibitor] versus response function
604 with variable slope.
605
606 **Western Blotting**

20

607   Approximately 1,000,000 cells of the appropriate cell type were drugged as described in
608   individual assays and then pelleted (500x g for 4 min) at 4 °C, resuspended in ice cold PBS,
609   pelleted again, and then resuspended in 150 µl lysis buffer (50 mM Tris-HCl pH 7.4, 150 mM
610   NaCl, 1mM EDTA, 1% v/v Triton X-100, 10% v/v glycerol, 1x cOmplete protease inhibitor
611   cocktail (Roche), and 1x PhosSTOP (Roche)). Cells were rotated for 30 min at 4 °C and then
612   spun at 12,000 g for 20 min to pellet cell debris. The supernatant was removed to a fresh tube
613   and protein concentration was measured using a bicinchoninic acid assay (BCA assay). Within
614   an experiment, total protein concentration was normalized to the least concentrated sample
615   (typically all values were within ~10% and in the 1 µg / µl range). 5x Laemmli loading buffer (250
616   mM Tris-HCl pH 6.8, 30% glycerol, 0.25% bromophenol blue, 10% SDS, 5% beta-
617   mercaptoethanol) was added to each sample. Samples were placed in a 99 °C heat block for 10
618   min. Equal protein content for each condition (targeting 10 µg) was run on 10% Mini-PROTEAN
619   TGX precast protein gels (Biorad). After electrophoresis, proteins were transferred onto a
620   nitrocellulose membrane. Primary antibody / blocking conditions for each protein of interest are
621   outlined in Table 3. Initial blocking is performed for 2 h. Primary antibody staining was
622   performed with gentle agitation at 4 °C overnight. After washing 4 times in the appropriate
623   blocking buffer, secondary antibody staining was performed for 1 h at room temperature and
624   then membranes were washed 3x with the appropriate blocking buffer and then 1x with TBS-T
625   or PBS-T as appropriate. Membranes were developed with SuperSignal West Dura (Thermo
626   Fisher Scientific). Developed membranes were imaged on a LI-COR Odyssey gel imager for
627   0.5-10 min depending on band intensity.
628
629   **FLAG Immunoprecipitation**
630   Approximately 25,000,000 cells were drugged as described, removed from the incubator after 3
631   h of treatment, and pelleted (3 min, 1000 x g) then resuspended in ice cold PBS then pelleted
632   again. Cells were then resuspended in 200 µl Lysis Buffer (25 mM HEPES pH 7.4, 150 mM KCl,
633   1% NP-40, 1 mM EDTA, 2.5x cOmplete protease inhibitor cocktail (Roche), and 1x PhosSTOP
634   (Roche)). Cells were vortexed for 3 s then incubated on ice for 3 min, with this process repeated
635   3 times. Cell debris was pelleted as described above, and the supernatant was removed to a
636   new tube. A portion was retained as the Cell Lysate fraction. The remaining cell lysate was
637   incubated at 4 °C overnight with M2 flag monoclonal antibody (Sigma Aldrich) conjugated to
638   magnetic Protein G Dynabeads (Invitrogen). Beads were washed 3x with 500 µl of Sample
639   Buffer (20 mM HEPES pH 7.4, 100 mM KCl, 5 mM $MgCl_2$, and 1 mM TCEP) and then eluted

640   using FLAG peptide at 200 μg / ml (eIF2B Bound fraction). Both fractions were then treated as

641   described above for Western blotting.

642

643   **gDNA isolation, PCR, and DNA gel of edited loci**

644   gDNA from parental and edited cells was isolated using the PureLink Genomic DNA Mini Kit

645   (Invitrogen) as per manufacturer instructions. The targeted *EIF2B1*, *EIF2B2*, and *EIF2B4* loci

646   were amplified with the primer pairs detailed in Table 4 and run on a 1% agarose gel and

647   imaged using a ChemiDoc XRS+ imaging system (Biorad). The expected WT fragment length

648   for the *EIF2B1*, *EIF2B2*, and *EIF2B4* products are 256, 151, and 224 bp, respectively, while the

649   edited products are expected at 643, 955, and 997 bp, respectively.

650

651   **Purification of human eIF2B subcomplexes**

652   Human eIFBα$_2$ (pJT075 or pMS027), eIF2Bβγδε (pJT073 and pJT074 co-expression), and

653   eIF2Bβγδε-F (pMS029 and pJT074 co-expression) were purified as previously described (Tsai

654   et al. 2018). All eIF2B(αβγδε)$_2$ used throughout was assembled by mixing purified eIF2Bβγδε

655   and eIF2Bα$_2$ at the appropriate molar ratios.

656

657   **Purification of human eIF2α and eIF2α-P**

658   The purification of human eIF2α was modified from a previous protocol (Kenner et al. 2019).

659   Briefly, the expression plasmid for N-terminally 6x-His-tagged human eIF2α, pAA007, was heat-

660   transformed into One Shot BL21 Star (DE3) chemically competent *E. coli* cells (Invitrogen),

661   along with the tetracycline-inducible, chloramphenicol-resistant plasmid, pG-Tf2, containing the

662   chaperones groES, groEL, and Tig (Takara Bio). Transformed cells were selected for in LB with

663   kanamycin and chloramphenicol. When the culture reached an OD600 of ~0.2, 1 ng / ml,

664   tetracycline was added to induce expression of chaperones. At an OD$_{600}$ of ~0.8, the culture

665   was cooled to room temperature, eIF2α expression was induced with 1 mM IPTG (Gold

666   Biotechnology) and the culture was grown for 16 hours at 16 °C. Cells were harvested and lysed

667   through 3 cycles of high-pressure homogenization using the EmulsiFlex-C3 (Avestin) in a buffer

668   containing 100 mM HEPES-KOH, pH 7.5, 300 mM KCl, 2 mM dithiothreitol (DTT), 5 mM MgCl$_2$,

669   5 mM imidazole, 10% glycerol, 0.1% IGEPAL CA-630, and cOmplete EDTA-free protease

670   inhibitor cocktail (Roche). The lysate was clarified at 30,000 x g for 30 min at 4 °C. Subsequent

671   purification steps were conducted on the ÄKTA Pure (GE Healthcare) system at 4 °C. Clarified

672   lysate was loaded onto a 5 ml HisTrap FF Crude column (GE Healthcare), washed in a buffer

673   containing 20 mM HEPES-KOH, pH 7.5, 100 mM KCl, 5% glycerol, 1 mM DTT, 5 mM MgCl$_2$,

674 0.1% IGEPAL CA-630, and 20 mM imidazole, and eluted with 75 ml linear gradient of 20 to 500

675 mM imidazole. The eIF2α-containing fractions were collected and applied to a MonoQ HR

676 10/100 GL column (GE Healthcare) equilibrated in a buffer containing 20 mM HEPES-KOH pH

677 7.5, 100 mM KCl, 1 mM DTT, 5% glycerol, and 5 mM $MgCl_2$ for anion exchange. The column

678 was washed in the same buffer, and the protein was eluted with an 80 ml linear gradient of 100

679 mM to 1 M KCl. eIF2α containing fractions were collected and concentrated with an Amicon

680 Ultra-15 concentrator (EMD Millipore) with a 30,000-dalton molecular mass cutoff, spun down

681 for 10 min at 10,000 g to remove aggregates. The supernatant was then chromatographed on a

682 Superdex 75 10/300 GL (GE Healthcare) column equilibrated in a buffer containing 20 mM

683 HEPES-KOH pH 7.5, 100 mM KCl, 1 mM DTT, 5 mM $MgCl_2$, and 5% glycerol, and concentrated

684 using Amicon Ultra-15 concentrators (EMD Millipore) with a 10,000-dalton molecular mass

685 cutoff.

686

687 For the purification of human phosphorylated eIF2α (eIF2α-P) the protein was expressed and

688 purified as described above for eIF2α, except that before size exclusion on the Superdex 75,

689 the pooled anion exchange fractions were phosphorylated *in vitro* overnight at 4 °C with 1 mM

690 ATP and 1 µg of $PKR_{(252-551)}$-GST enzyme (Thermo Scientific) per mg of eIF2α. Complete

691 phosphorylation was confirmed by running the samples on a 12.5% Super-Sep PhosTag gel

692 (Wako Chemicals).

693

694 **Purification of heterotrimeric human eIF2 and eIF2-P**

695 Human eIF2 was prepared from an established recombinant *S. cerevisiae* expression protocol

696 (de Almeida et al. 2013). In brief, the yeast strain GP6452 (gift from the Pavitt lab, University of

697 Manchester) containing yeast expression plasmids for human eIF2 subunits and a deletion of

698 GCN2 encoding the only eIF2 kinase in yeast, was grown to saturation in synthetic complete

699 media (Sunrise Science Products) with auxotrophic markers (-Trp, -Leu, -Ura) in 2% dextrose.

700 The β and α subunits of eIF2 were tagged with 6x-His and FLAG epitopes, respectively. A 12

701 liter yeast culture was grown in rich expression media containing yeast extract, peptone, 2%

702 galactose, and 0.2% dextrose. Cells were harvested and resuspended in lysis buffer (100 mM

703 Tris, pH 8.5, 300 mM KCl, 5 mM $MgCl_2$, 0.1% NP-40, 5 mM imidazole, 10% glycerol (Thermo

704 Fisher Scientific), 1 mM TCEP, 1x cOmplete protease inhibitor cocktail (Sigma Aldrich), 1 µg /

705 ml each aprotinin (Sigma Aldrich), leupeptin (Sigma Aldrich), pepstatin A (Sigma Aldrich)). Cells

706 were lysed in liquid nitrogen using a steel blender. The lysate was centrifuged at 30,000 x g for

707 30 min at 4 °C. Subsequent purification steps were conducted on the ÄKTA Pure (GE

708   Healthcare) system at 4 °C. Lysate was applied to a 5 ml HisTrap FF Crude column (GE

709   Healthcare) equilibrated in buffer (100 mM HEPES-KOH, pH 7.5, 100 mM KCl, 5 mM $MgCl_2$,

710   0.1% NP-40, 5% glycerol, 1 mM TCEP, 0.5x cOmplete protease inhibitor cocktail, 1 µg/ml each

711   aprotinin, leupeptin, pepstatin A). eIF2 bound to the column was washed with equilibration

712   buffer and eluted using a 50 ml linear gradient of 5 mM to 500 mM imidazole. Eluted eIF2 was

713   incubated with FLAG M2 magnetic affinity beads, washed with FLAG wash buffer (100 mM

714   HEPES-KOH, pH 7.5, 100 mM KCl, 5 mM $MgCl_2$, 0.1% NP-40, 5% glycerol, 1 mM TCEP, 1x

715   cOmplete protease inhibitor cocktail, 1 µg/ml each aprotinin, leupeptin, pepstatin A) and eluted

716   with FLAG elution buffer [identical to FLAG wash buffer but also containing 3x FLAG peptide

717   (100 µg/ml, Sigma Aldrich)]. Protein was flash-frozen in liquid nitrogen and stored in elution

718   buffer at -80 °C.

719

720   For the purification of eIF2-P the protein was purified as above, except that a final concentration

721   of 10 nM recombinant PKR (Life Technologies # PV4821) and 1 mM ATP was added during

722   incubation with FLAG M2 magnetic beads. These components were removed during the wash

723   steps described above. Phosphorylation of the final product was verified by 12.5% SuperSep

724   PhosTag gel (Wako Chemical Corporation).

725

726   Additional human eIF2 was purified as previously described with the only modification in one

727   purification being an additional Avi-Tag on the eIF2α subunit (Wong et al. 2018). This material

728   was a generous gift of Carmela Sidrauski and Calico Life Sciences.

729

730   ***In vitro* eIF2/eIF2α-P immunoprecipitation**

731   eIF2B(αβδγε)$_2$ decamers were assembled by mixing eIF2Bβγδε and protein C-tagged eIF2Bα$_2$

732   in a 2:1 molar ratio and incubating at room temperature for at least 1 hour. Varying

733   combinations of purified eIF2, eIF2α-P, eIF2B(αβδγε)$_2$, and ISRIB were incubated (with gentle

734   rocking) with Anti-protein C antibody conjugated resin (generous gift from Aashish Manglik) in

735   Assay Buffer (20 mM HEPES-KOH, pH 7.5, 150 mM KCl, 5 mM $MgCl_2$, 1mM TCEP, 1 mg/ml

736   bovine serum albumin (BSA), 5mM $CaCl_2$). After 1.5 hours the resin was pelleted by benchtop

737   centrifugation and the supernatant was removed. Resin was washed 3x with 1 mL of ice cold

738   Assay Buffer before resin was resuspended in Elution Buffer (Assay Buffer with 5 mM EDTA

739   and 0.5 mg/mL protein C peptide added) and incubated with gentle rocking for 1 hour. The resin

740   was then pelleted and the supernatant was removed. Samples were analyzed by Western

741   Blotting as previously described

Analytical ultracentrifugation

Analytical ultracentrifugation sedimentation velocity experiments were performed as previously described (Tsai et al. 2018).

In vitro **FRET assays**

Equilibrium measurements of eIF2B assembly state were performed in 20 µl reactions with 50 nM eIF2Bβγδε-F + ISRIB or eIF2Bα$_2$ titrations in FP buffer (20 mM HEPES-KOH pH 7.5, 100 mM KCl, 5 mM MgCl$_2$, 1 mM TCEP) and measured in 384 square-well black-walled, clear-bottom polystyrene assay plates (Corning). Measurements were taken using the ClarioStar PLUS plate reader (BMG LabTech) at room temperature. mNeonGreen was excited (470 nm, 8 nm bandwidth) and mNeonGreen (516 nm, 8 nm bandwidth) and mScarlet-i (592 nm, 8 nm bandwidth) emission were monitored. FRET signal (E_{592}/E_{516}) is the ratio of mScarlet-i emission after mNeonGreen excitation and mNeonGreen emission after mNeonGreen excitation. All reactions were performed in a final 0.5% DMSO content. Samples were incubated for 1 h before measurement. Data were plotted in GraphPad Prism 8 and curves were fit to log(inhibitor) versus response function with variable slope.

Kinetic measurements of eIF2B assembly were performed in the same final volume and buffer as above. 10 µl of 2x ISRIB, eIF2Bα$_2$, or ISRIB + eIF2Bα$_2$ stocks were placed in wells of the above-described assay plate. 10 µl of 100 nM (2x) eIF2Bβγδε-F was then added and mixed with the contents of each well using a 20 µl 12-channel multichannel pipette. Measurements were taken using the above instrument every 18 s for the first 24 cycles and then every 45 s for the next 60 cycles. mNeonGreen was excited (470 nm, 16 nm bandwidth), and mNeonGreen (516 nm, 16 nm bandwidth) and mScarlet-i (592 nm, 16 nm bandwidth) emission were monitored. After this association phase 18 μl were removed from each well using a multichannel pipette and mixed with 1 µl of 20 µM (20x) untagged eIF2Bβγδε pre-loaded into PCR strips. The material was then returned to the original wells and measurement of dissociation began. Measurements were taken every 18 s for the first 24 cycles and then every 45 s for the next 120 cycles. Data were plotted in GraphPad Prism 8. Association and dissociation phases were fit separately using the One-phase association and Dissociation – One phase exponential decay models, respectively. Global fits were performed on the ISRIB titrations or eIF2Bα$_2$ titrations. When modeling dissociation, the median buffer signal at assay completion was used to set the bottom baseline for conditions where full dissociation was not observed (eIF2Bα$_2$ and eIF2Bα$_2$ + ISRIB conditions).

775

GDP exchange assay

in vitro detection of GDP binding to eIF2 was adapted from a published protocol for a
fluorescence intensity–based assay describing dissociation of eIF2 and nucleotide (Sekine et al.
2015). We first performed a loading assay for fluorescent BODIPY-FL-GDP as described (Tsai
et al. 2018). Purified eIF2 (100 nM) was incubated with 100 nM BODIPY-FL-GDP (Thermo
Fisher Scientific) in assay buffer (20 mM HEPES-KOH, pH 7.5, 100 mM KCl, 5 mM $MgCl_2$, 1
mM TCEP, and 1 mg/ml BSA) to a volume of 18 µl in 384 square-well black-walled, clear-
bottom polystyrene assay plates (Corning). The GEF mix was prepared by incubating a 10x
solution of eIF2B($\alpha\beta\gamma\delta\epsilon$)$_2$ with 10x solutions of eIF2-P or eIF2α-P. For analyzing the effect of
ISRIB, the 10x GEF mixes were pre-incubated with 2% NMP or 10 µM ISRIB in N-Methyl-2-
Pyrrolidone (NMP), such that the final NMP and ISRIB concentration was 1 µM and the final
NMP concentration was 0.2%. To compare nucleotide exchange rates, the 10x GEF mixes were
spiked into the 384-well plate wells with a multi-channel pipette, such that the resulting final
concentration of eIF2B($\alpha\beta\gamma\delta\epsilon$)$_2$ was 10 nM and the final concentration of other proteins and
drugs are as indicated in the figures. Subsequently, in the same wells, we performed a "GDP
unloading assay," as indicated in the figures. After completion of the loading reaction, wells
were next spiked with 1 mM GDP to start the unloading reaction at t = 0. Fluorescence intensity
was recorded every 10 s for 60 min using a Clariostar PLUS (BMG LabTech) plate reader
(excitation wavelength: 497 nm, bandwidth 14 nm, emission wavelength: 525 nm, bandwidth: 30
nm). Data collected were fit to a first-order exponential.

Michaelis Menten kinetics

BODIPY-FL-GDP loading assays were performed as described above, varying substrate
concentration in 2-fold increments from 31.25 nM to 4 µM while eIF2B decamer concentration
was held constant at 10 nM. Experiments containing tetramer were performed at 20 nM, such
that the number of active sites was held constant. For conditions reported in Figure 6A, initial
velocity was determined by a linear fit to timepoints acquired at 5 second intervals from 50 –
200 seconds after addition of GEF. For eIF2B tetramer and eIF2B decamer + 15 µM eIF2α-P
conditions, timepoints were acquired at 20 second intervals and initial velocity was determined
by a linear fit to timepoints 400 - 1000 seconds. k_{cat} and K_M were determined by fitting the
saturation curves shown in Fig. 6A to the Michaelis Menten equation. Data collected for
tetramer and decamer + 15 µM eIF2α-P conditions fell within the linear portion of the Michaelis

808   Menten saturation curve, and thus the linear portion of each curve was fit to determine the k_{cat} /

809   K_M values reported in Figure 6B.

810

811   **FAM-ISRIB binding assay**

812   All fluorescence polarization measurements were performed in 20 µl reactions with 100 nM

813   eIF2B(αβγδε)$_2$ + 2.5 nM FAM-ISRIB (Praxis Bioresearch) in FP buffer (20 mM HEPES-KOH pH

814   7.5, 100 mM KCl, 5 mM MgCl$_2$, 1 mM TCEP) and measured in 384-well non-stick black plates

815   (Corning 3820) using the ClarioStar PLUS (BMG LabTech) at room temperature. Prior to

816   reaction setup, eIF2B(αβγδε)$_2$ was assembled in FP buffer using eIF2Bβγδε and eIF2Bα$_2$ in 2:1

817   molar ratio for at least 15 min at room temperature. FAM-ISRIB was always first diluted to 2.5

818   µM in 100% NMP prior to dilution to 50 nM in 2% NMP and then added to the reaction. For

819   titrations with eIF2, eIF2-P, eIF2α, and eIF2α-P, dilutions were again made in FP buffer, and the

820   reactions with eIF2B, FAM-ISRIB, and these dilutions were incubated at 22 °C for 30 min prior

821   to measurement of parallel and perpendicular intensities (excitation: 482 nm, emission: 530

822   nm). To measure the effect of phosphorylated eIF2 on FAM-ISRIB binding to eIF2B, we

823   additionally added 1 µl (0.21 µg) of PKR$_{(252-551)}$-GST enzyme (Thermo Scientific) and 1 mM ATP

824   to the reaction with eIF2B, FAM-ISRIB and eIF2 before incubation at 22 °C for 30 min. For the

825   measurement of eIF2 and eIF2α-P competition, 19 µl reactions of 100 nM eIF2B(αβγδε)$_2$, 2.5

826   nM FAM-ISRIB, and 6 µM eIF2α-P were incubated with titrations of eIF2 for 30 min before

827   polarization was measured. To confirm that FAM-ISRIB binding was specific to eIF2B, after

828   each measurement, ISRIB was spiked to 1 µM into each reaction (from a 40 µM stock in 100%

829   NMP), reactions were incubated for 15 min at 22 °C, and polarization was measured again

830   using the same gain settings. Data were plotted in GraphPad Prism 8, and where appropriate,

831   curves were fit to log[inhibitor] vs response function with variable slope.

832

833   The kinetic characterization of FAM-ISRIB binding during eIF2α phosphorylation was assayed in

834   19 µl reactions of 100 nM eIF2B(αβγδε)$_2$, 2.5 nM FAM-ISRIB, 1 mM ATP, and 5.6 µM eIF2α /

835   eIF2α-P in FP buffer. These solutions were pre-incubated at 22 °C for 30 min before

836   polarization was measured every 15 s (30 flashes / s). After 4 cycles, 1 µl (0.21 µg) of PKR$_{(252-}$

837    $_{551)}$-GST enzyme (Thermo Scientific) was added, and measurement was resumed.

838   Dephosphorylation reactions were set up in an analogous way, but instead of ATP 1 mM MnCl$_2$

839   was added and 1 µl (400 U) of λ phosphatase (NEB) was used instead of PKR.

840

841   **Sample preparation for cryo-electron microscopy**

842   Decameric eIF2B(αβγδε)$_2$ was prepared by incubating 20 μM eIF2Bβγδε with 11 μM eIF2Bα$_2$ in

843   a final solution containing 20 mM HEPES-KOH, 200 mM KCl, 5 mM MgCl$_2$, and 1 mM TCEP.

844   This 10 μM eIF2B(αβγδε)$_2$ sample was further diluted to 750 nM and incubated on ice for 1 h

845   before plunge freezing. A 3 μl aliquot of the sample was applied onto the Quantifoil R 1.2/1/3

846   400 mesh Gold grid and waited for 30 s. A 0.5 μl aliquot of 0.1-0.2% Nonidet P-40 substitute

847   was added immediately before blotting. The entire blotting procedure was performed using

848   Vitrobot (FEI) at 10°C and 100% humidity.

849

850   **Electron microscopy data collection**

851   Cryo-EM data for the *apo* decamer of eIF2B was collected on a Titan Krios transmission

852   electron microscope operating at 300 keV, and micrographs were acquired using a Gatan K3

853   direct electron detector. The total dose was 67 e$^-$/Å^2, and 117 frames were recorded during a

854   5.9 s exposure. Data was collected at 105,000 x nominal magnification (0.835 Å/pixel at the

855   specimen level), and nominal defocus range of -0.6 to -2.0 μm. Cryo-EM data for the ISRIB-

856   bound eIF2B decamer (EMDB:7442, 7443, and 7444) (Tsai et al. 2018) and the eIF2-bound

857   eIF2B decamer were collected as described previously (EMDB:0651) (Kenner et al. 2019).

858

859   **Image processing**

860   For the apo decamer, the micrograph frames were aligned using MotionCorr2 (Zheng et al.

861   2017). The contrast transfer function (CTF) parameters were estimated with GCTF (Zhang

862   2016). Particles were automatically picked using Gautomatch and extracted in RELION using a

863   400-pixel box size (Scheres 2012). Particles were classified in 2D in Cryosparc (Punjani et al.

864   2017). Classes that showed clear protein features were selected and extracted for

865   heterogeneous refinement using the ISRIB-bound decamer as a starting model (EMDB ID:

866   7442) (Tsai et al. 2018). Homogeneous refinement was performed on the best model to yield a

867   reconstruction of 2.89 Å. Nonuniform refinement was then performed to yield a final

868   reconstruction of 2.83 Å. For the ISRIB-bound eIF2B decamer (EMDB:7442, 7443, and 7444)

869   (Tsai et al. 2018), and the eIF2-bound eIF2B decamer (EMDB:0651) (Kenner et al. 2019), the

870   published maps were used for further model refinement.

871

872   **Atomic model building, refinement, and visualization**

873   For all models, previously determined structures of the human eIF2B complex [PDB: 6CAJ]

874   (Tsai et al. 2018), human eIF2α [PDBs: 1Q8K (Ito, Marintchev, and Wagner 2004) and 1KL9

875   (Nonato, Widom, and Clardy 2002)], the C-terminal HEAT domain of eIF2Bε [PDB: 3JUI (Wei et

28

876 al. 2010)], and mammalian eIF2γ [PDB: 5K0Y (Esser et al. 2017)] were used for initial atomic

877 interpretation. The models were manually adjusted in Coot (Emsley and Cowtan 2004) or

878 ISOLDE (Croll 2018) and then refined in phenix.real_space_refine (Adams et al. 2010) using

879 global minimization, secondary structure restraints, Ramachandran restraints, and local grid

880 search. Then iterative cycles of manually rebuilding in Coot and phenix.real_space_refine with

881 additional B-factor refinement were performed. The final model statistics were tabulated using

882 Molprobity (Table 1 and 2) (Chen et al. 2010). Map versus atomic model FSC plots were

883 computed after masking using Phenix validation tools. Distances and rotations were calculated

884 from the atomic models using UCSF Chimera. Final atomic models have been deposited at the

885 PDB with the following accession codes: ISRIB-bound eIF2B (6caj, updated), eIF2•eIF2B•ISRIB

886 (6o85); and apo eIF2B (7L70). Molecular graphics and analyses were performed with the UCSF

887 Chimera package (Pettersen et al. 2004). UCSF Chimera is developed by the Resource for

888 Biocomputing, Visualization, and Informatics and supported by NIGMS P41-GM103311.

889

905

906 **Competing Interests**

907 PW is an inventor on U.S. Patent 9708247 held by the Regents of the University of California

908 that describes ISRIB and its analogs. Rights to the invention have been licensed by UCSF to

909 Calico. For the remaining authors, no competing financial interests exist.

References

Adams, P. D., P. V. Afonine, G. Bunkóczi, V. B. Chen, I. W. Davis, N. Echols, J. J. Headd, L. W. Hung, G. J. Kapral, R. W. Grosse-Kunstleve, A. J. McCoy, N. W. Moriarty, R. Oeffner, R. J. Read, D. C. Richardson, J. S. Richardson, T. C. Terwilliger, and P. H. Zwart. 2010. 'PHENIX: a comprehensive Python-based system for macromolecular structure solution', *Acta Crystallogr D Biol Crystallogr*, 66: 213-21.

Adomavicius, T., M. Guaita, Y. Zhou, M. D. Jennings, Z. Latif, A. M. Roseman, and G. D. Pavitt. 2019. 'The structural basis of translational control by eIF2 phosphorylation', *Nat Commun*, 10: 2136.

Algire, M. A., D. Maag, and J. R. Lorsch. 2005. 'Pi release from eIF2, not GTP hydrolysis, is the step controlled by start-site selection during eukaryotic translation initiation', *Mol Cell*, 20: 251-62.

Atkin, J. D., M. A. Farg, A. K. Walker, C. McLean, D. Tomas, and M. K. Horne. 2008. 'Endoplasmic reticulum stress and induction of the unfolded protein response in human sporadic amyotrophic lateral sclerosis', *Neurobiol Dis*, 30: 400-7.

Bogorad, A. M., K. Y. Lin, and A. Marintchev. 2017. 'Novel mechanisms of eIF2B action and regulation by eIF2α phosphorylation', *Nucleic Acids Res*, 45: 11962-79.

Chen, V. B., W. B. Arendall, 3rd, J. J. Headd, D. A. Keedy, R. M. Immormino, G. J. Kapral, L. W. Murray, J. S. Richardson, and D. C. Richardson. 2010. 'MolProbity: all-atom structure validation for macromolecular crystallography', *Acta Crystallogr D Biol Crystallogr*, 66: 12-21.

Chou, A., K. Krukowski, T. Jopson, P. J. Zhu, M. Costa-Mattioli, P. Walter, and S. Rosi. 2017. 'Inhibition of the integrated stress response reverses cognitive deficits after traumatic brain injury', *Proc Natl Acad Sci U S A*, 114: E6420-e26.

Costa-Mattioli, M., and P. Walter. 2020. 'The integrated stress response: From mechanism to disease', *Science*, 368.

Craddock, B. L., and C. G. Proud. 1996. 'The alpha-subunit of the mammalian guanine nucleotide-exchange factor eIF-2B is essential for catalytic activity in vitro', *Biochem Biophys Res Commun*, 220: 843-7.

Croll, T. I. 2018. 'ISOLDE: a physically realistic environment for model building into low-resolution electron-density maps', *Acta Crystallogr D Struct Biol*, 74: 519-30.

de Almeida, R. A., A. Fogli, M. Gaillard, G. C. Scheper, O. Boesflug-Tanguy, and G. D. Pavitt. 2013. 'A yeast purification system for human translation initiation factors eIF2 and eIF2Bε and their use in the diagnosis of CACH/VWM disease', *PLoS One*, 8: e53958.

Dey, M., C. Cao, A. C. Dar, T. Tamura, K. Ozato, F. Sicheri, and T. E. Dever. 2005. 'Mechanistic link between PKR dimerization, autophosphorylation, and eIF2alpha substrate recognition', *Cell*, 122: 901-13.

Elsby, R., J. F. Heiber, P. Reid, S. R. Kimball, G. D. Pavitt, and G. N. Barber. 2011. 'The alpha subunit of eukaryotic initiation factor 2B (eIF2B) is required for eIF2-mediated translational suppression of vesicular stomatitis virus', *J Virol*, 85: 9716-25.

Emsley, P., and K. Cowtan. 2004. 'Coot: model-building tools for molecular graphics', *Acta Crystallogr D Biol Crystallogr*, 60: 2126-32.

Esser, L., F. Zhou, K. M. Pluchino, J. Shiloach, J. Ma, W. K. Tang, C. Gutierrez, A. Zhang, S. Shukla, J. P. Madigan, T. Zhou, P. D. Kwong, S. V. Ambudkar, M. M. Gottesman, and D. Xia. 2017. 'Structures of the Multidrug Transporter P-glycoprotein Reveal

956   Asymmetric ATP Binding and the Mechanism of Polyspecificity', *J Biol Chem*, 292:
957   446-61.
958 Gilbert, L. A., M. A. Horlbeck, B. Adamson, J. E. Villalta, Y. Chen, E. H. Whitehead, C.
959   Guimaraes, B. Panning, H. L. Ploegh, M. C. Bassik, L. S. Qi, M. Kampmann, and J. S.
960   Weissman. 2014. 'Genome-Scale CRISPR-Mediated Control of Gene Repression and
961   Activation', *Cell*, 159: 647-61.
962 Gordiyenko, Y., J. L. Llácer, and V. Ramakrishnan. 2019. 'Structural basis for the inhibition of
963   translation through eIF2α phosphorylation', *Nat Commun*, 10: 2640.
964 Guo, X., G. Aviles, Y. Liu, R. Tian, B. A. Unger, Y. T. Lin, A. P. Wiita, K. Xu, M. A. Correia, and M.
965   Kampmann. 2020. 'Mitochondrial stress is relayed to the cytosol by an OMA1-
966   DELE1-HRI pathway', *Nature*, 579: 427-32.
967 Hannig, E. M., and A. G. Hinnebusch. 1988. 'Molecular analysis of GCN3, a translational
968   activator of GCN4: evidence for posttranslational control of GCN3 regulatory
969   function', *Mol Cell Biol*, 8: 4808-20.
970 Harding, H. P., I. Novoa, Y. Zhang, H. Zeng, R. Wek, M. Schapira, and D. Ron. 2000. 'Regulated
971   translation initiation controls stress-induced gene expression in mammalian cells',
972   *Mol Cell*, 6: 1099-108.
973 Harding, H. P., Y. Zhang, H. Zeng, I. Novoa, P. D. Lu, M. Calfon, N. Sadri, C. Yun, B. Popko, R.
974   Paules, D. F. Stojdl, J. C. Bell, T. Hettmann, J. M. Leiden, and D. Ron. 2003. 'An
975   integrated stress response regulates amino acid metabolism and resistance to
976   oxidative stress', *Mol Cell*, 11: 619-33.
977 Hinnebusch, A. G. 2005. 'Translational regulation of GCN4 and the general amino acid
978   control of yeast', *Annu Rev Microbiol*, 59: 407-50.
979 Hinnebusch, A. G., I. P. Ivanov, and N. Sonenberg. 2016. 'Translational control by 5'-
980   untranslated regions of eukaryotic mRNAs', *Science*, 352: 1413-6.
981 Ito, T., A. Marintchev, and G. Wagner. 2004. 'Solution structure of human initiation factor
982   eIF2alpha reveals homology to the elongation factor eEF1B', *Structure*, 12: 1693-
983   704.
984 Iwamoto, M., T. Björklund, C. Lundberg, D. Kirik, and T. J. Wandless. 2010. 'A general
985   chemical method to regulate protein stability in the mammalian central nervous
986   system', *Chem Biol*, 17: 981-8.
987 Kashiwagi, K., M. Takahashi, M. Nishimoto, T. B. Hiyama, T. Higo, T. Umehara, K. Sakamoto,
988   T. Ito, and S. Yokoyama. 2016. 'Crystal structure of eukaryotic translation initiation
989   factor 2B', *Nature*, 531: 122-5.
990 Kashiwagi, K., T. Yokoyama, M. Nishimoto, M. Takahashi, A. Sakamoto, M. Yonemochi, M.
991   Shirouzu, and T. Ito. 2019. 'Structural basis for eIF2B inhibition in integrated stress
992   response', *Science*, 364: 495-99.
993 Kenner, L. R., A. A. Anand, H. C. Nguyen, A. G. Myasnikov, C. J. Klose, L. A. McGeever, J. C. Tsai,
994   L. E. Miller-Vedam, P. Walter, and A. Frost. 2019. 'eIF2B-catalyzed nucleotide
995   exchange and phosphoregulation by the integrated stress response', *Science*, 364:
996   491-95.
997 Krukowski, K., A. Nolan, E. S. Frias, M. Boone, G. Ureta, K. Grue, M. S. Paladini, E. Elizarraras,
998   L. Delgado, S. Bernales, P. Walter, and S. Rosi. 2020. 'Small molecule cognitive
999   enhancer reverses age-related memory decline in mice', *Elife*, 9.

1000   Kuhle, B., N. K. Eulig, and R. Ficner. 2015. 'Architecture of the eIF2B regulatory subcomplex
1001   and its implications for the regulation of guanine nucleotide exchange on eIF2',
1002   *Nucleic Acids Res*, 43: 9994-10014.
1003   Leegwater, P. A., G. Vermeulen, A. A. Könst, S. Naidu, J. Mulders, A. Visser, P. Kersbergen, D.
1004   Mobach, D. Fonds, C. G. van Berkel, R. J. Lemmers, R. R. Frants, C. B. Oudejans, R. B.
1005   Schutgens, J. C. Pronk, and M. S. van der Knaap. 2001. 'Subunits of the translation
1006   initiation factor eIF2B are mutant in leukoencephalopathy with vanishing white
1007   matter', *Nat Genet*, 29: 383-8.
1008   Leonetti, M. D., S. Sekine, D. Kamiyama, J. S. Weissman, and B. Huang. 2016. 'A scalable
1009   strategy for high-throughput GFP tagging of endogenous human proteins', *Proc Natl
1010   Acad Sci U S A*, 113: E3501-8.
1011   Ma, T., M. A. Trinh, A. J. Wexler, C. Bourbon, E. Gatti, P. Pierre, D. R. Cavener, and E. Klann.
1012   2013. 'Suppression of eIF2α kinases alleviates Alzheimer's disease-related plasticity
1013   and memory deficits', *Nat Neurosci*, 16: 1299-305.
1014   Nabet, B., J. M. Roberts, D. L. Buckley, J. Paulk, S. Dastjerdi, A. Yang, A. L. Leggett, M. A. Erb,
1015   M. A. Lawlor, A. Souza, T. G. Scott, S. Vittori, J. A. Perry, J. Qi, G. E. Winter, K. K. Wong,
1016   N. S. Gray, and J. E. Bradner. 2018. 'The dTAG system for immediate and target-
1017   specific protein degradation', *Nat Chem Biol*, 14: 431-41.
1018   Nguyen, H. G., C. S. Conn, Y. Kye, L. Xue, C. M. Forester, J. E. Cowan, A. C. Hsieh, J. T.
1019   Cunningham, C. Truillet, F. Tameire, M. J. Evans, C. P. Evans, J. C. Yang, B. Hann, C.
1020   Koumenis, P. Walter, P. R. Carroll, and D. Ruggero. 2018. 'Development of a stress
1021   response therapy targeting aggressive prostate cancer', *Sci Transl Med*, 10.
1022   Nonato, M. C., J. Widom, and J. Clardy. 2002. 'Crystal structure of the N-terminal segment of
1023   human eukaryotic translation initiation factor 2alpha', *J Biol Chem*, 277: 17057-61.
1024   Pavitt, G. D., W. Yang, and A. G. Hinnebusch. 1997. 'Homologous segments in three subunits
1025   of the guanine nucleotide exchange factor eIF2B mediate translational regulation by
1026   phosphorylation of eIF2', *Mol Cell Biol*, 17: 1298-313.
1027   Pettersen, E. F., T. D. Goddard, C. C. Huang, G. S. Couch, D. M. Greenblatt, E. C. Meng, and T. E.
1028   Ferrin. 2004. 'UCSF Chimera--a visualization system for exploratory research and
1029   analysis', *J Comput Chem*, 25: 1605-12.
1030   Punjani, A., J. L. Rubinstein, D. J. Fleet, and M. A. Brubaker. 2017. 'cryoSPARC: algorithms for
1031   rapid unsupervised cryo-EM structure determination', *Nat Methods*, 14: 290-96.
1032   Rabouw, H. H., L. J. Visser, T. C. Passchier, M. A. Langereis, F. Liu, P. Giansanti, A. L. W. van
1033   Vliet, J. G. Dekker, S. G. van der Grein, J. G. Saucedo, A. A. Anand, M. E. Trellet, Amjj
1034   Bonvin, P. Walter, A. J. R. Heck, R. J. de Groot, and F. J. M. van Kuppeveld. 2020.
1035   'Inhibition of the integrated stress response by viral proteins that block p-eIF2-
1036   eIF2B association', *Nat Microbiol*, 5: 1361-73.
1037   Scheres, S. H. 2012. 'RELION: implementation of a Bayesian approach to cryo-EM structure
1038   determination', *J Struct Biol*, 180: 519-30.
1039   Sekine, Y., A. Zyryanova, A. Crespillo-Casado, P. M. Fischer, H. P. Harding, and D. Ron. 2015.
1040   'Stress responses. Mutations in a translation initiation factor identify the target of a
1041   memory-enhancing compound', *Science*, 348: 1027-30.
1042   Sen, T., R. Gupta, H. Kaiser, and N. Sen. 2017. 'Activation of PERK Elicits Memory
1043   Impairment through Inactivation of CREB and Downregulation of PSD95 After
1044   Traumatic Brain Injury', *J Neurosci*, 37: 5900-11.

1045 Sharma, V., H. Ounallah-Saad, D. Chakraborty, M. Hleihil, R. Sood, I. Barrera, E. Edry, S.
1046   Kolatt Chandran, S. Ben Tabou de Leon, H. Kaphzan, and K. Rosenblum. 2018. 'Local
1047   Inhibition of PERK Enhances Memory and Reverses Age-Related Deterioration of
1048   Cognitive and Neuronal Properties', *J Neurosci*, 38: 648-58.
1049 Shi, Y., K. M. Vattem, R. Sood, J. An, J. Liang, L. Stramm, and R. C. Wek. 1998. 'Identification
1050   and characterization of pancreatic eukaryotic initiation factor 2 alpha-subunit
1051   kinase, PEK, involved in translational control', *Mol Cell Biol*, 18: 7499-509.
1052 Sidrauski, C., D. Acosta-Alvear, A. Khoutorsky, P. Vedantham, B. R. Hearn, H. Li, K. Gamache,
1053   C. M. Gallagher, K. K. Ang, C. Wilson, V. Okreglak, A. Ashkenazi, B. Hann, K. Nader, M.
1054   R. Arkin, A. R. Renslo, N. Sonenberg, and P. Walter. 2013. 'Pharmacological brake-
1055   release of mRNA translation enhances cognitive memory', *Elife*, 2: e00498.
1056 Sidrauski, C., J. C. Tsai, M. Kampmann, B. R. Hearn, P. Vedantham, P. Jaishankar, M. Sokabe,
1057   A. S. Mendez, B. W. Newton, E. L. Tang, E. Verschueren, J. R. Johnson, N. J. Krogan, C.
1058   S. Fraser, J. S. Weissman, A. R. Renslo, and P. Walter. 2015. 'Pharmacological
1059   dimerization and activation of the exchange factor eIF2B antagonizes the integrated
1060   stress response', *Elife*, 4: e07314.
1061 Tsai, J. C., L. E. Miller-Vedam, A. A. Anand, P. Jaishankar, H. C. Nguyen, A. R. Renslo, A. Frost,
1062   and P. Walter. 2018. 'Structure of the nucleotide exchange factor eIF2B reveals
1063   mechanism of memory-enhancing molecule', *Science*, 359.
1064 van der Knaap, M. S., P. A. Leegwater, A. A. Könst, A. Visser, S. Naidu, C. B. Oudejans, R. B.
1065   Schutgens, and J. C. Pronk. 2002. 'Mutations in each of the five subunits of
1066   translation initiation factor eIF2B can cause leukoencephalopathy with vanishing
1067   white matter', *Ann Neurol*, 51: 264-70.
1068 Wei, J., M. Jia, C. Zhang, M. Wang, F. Gao, H. Xu, and W. Gong. 2010. 'Crystal structure of the
1069   C-terminal domain of the ε subunit of human translation initiation factor eIF2B',
1070   *Protein Cell*, 1: 595-603.
1071 Wong, Y. L., L. LeBon, R. Edalji, H. B. Lim, C. Sun, and C. Sidrauski. 2018. 'The small molecule
1072   ISRIB rescues the stability and activity of Vanishing White Matter Disease eIF2B
1073   mutant complexes', *Elife*, 7.
1074 Wortham, N. C., M. Martinez, Y. Gordiyenko, C. V. Robinson, and C. G. Proud. 2014. 'Analysis
1075   of the subunit organization of the eIF2B complex reveals new insights into its
1076   structure and regulation', *Faseb j*, 28: 2225-37.
1077 Zhang, K. 2016. 'Gctf: Real-time CTF determination and correction', *J Struct Biol*, 193: 1-12.
1078 Zheng, S. Q., E. Palovcak, J. P. Armache, K. A. Verba, Y. Cheng, and D. A. Agard. 2017.
1079   'MotionCor2: anisotropic correction of beam-induced motion for improved cryo-
1080   electron microscopy', *Nat Methods*, 14: 331-32.
1081 Zhu, P. J., S. Khatiwada, Y. Cui, L. C. Reineke, S. W. Dooling, J. J. Kim, W. Li, P. Walter, and M.
1082   Costa-Mattioli. 2019. 'Activation of the ISR mediates the behavioral and
1083   neurophysiological abnormalities in Down syndrome', *Science*, 366: 843-49.
1084 Zyryanova, A. F., K. Kashiwagi, C. Rato, H. P. Harding, A. Crespillo-Casado, L. A. Perera, A.
1085   Sakamoto, M. Nishimoto, M. Yonemochi, M. Shirouzu, T. Ito, and D. Ron. 2021. 'ISRIB
1086   Blunts the Integrated Stress Response by Allosterically Antagonising the Inhibitory
1087   Effect of Phosphorylated eIF2 on eIF2B', *Mol Cell*, 81: 88-103.e6.
1088 Zyryanova, A. F., F. Weis, A. Faille, A. A. Alard, A. Crespillo-Casado, Y. Sekine, H. P. Harding,
1089   F. Allen, L. Parts, C. Fromont, P. M. Fischer, A. J. Warren, and D. Ron. 2018. 'Binding of

1090   ISRIB reveals a regulatory site in the nucleotide exchange factor eIF2B', *Science,* 359:
1091   1533-36.

1092

1093

1094

1095

1096

1097

1098

1099

1100

1101

1102

1103

1104

1105

1106

1107

1108

1109

1110   **Figure Legend**

1111

1112   **Figure 1**

1113   Cellular eIF2B assembly state in cells modulates the ISR. **(A)** Schematic of eIF2B assembly

1114   state modulation via the FKBP12^{F36V} / dTag13 system used to induce degradation of eIF2Bα.

1115   **(B)** Western blot of K562 cell extracts after treatment with thapsigargin (tg) or dTag13 for 3 h as

1116   indicated. Thapsigargin induces the ISR by depleting Ca^{2+} levels in the endoplasmic reticulum.

1117   Loading of all lanes was normalized to total protein. **(C-E)** ATF4 reporter levels as monitored by

1118   flow cytometry. Trimethoprim was at 20 μM. (C) Samples after 3 h of dTag13 treatment (EC_{50} =

1119   15 nM; s.e.m = 1 nM). (D) Samples after 3 h of ISRIB treatment +/- 83 nM dTag13 (EC_{50} = 1.4

1120   nM; s.e.m = 0.3 nM). (E**)** Timecourse of tg treatment (dTag13 = 83 nM, tg = 100 nM, ISRIB = 2

1121   μM).

1122   For (B), eIF2Bδ, eIF2Bα, and GAPDH blots, and the ATF4 and eIF2α blots are from the same

1123   gels, respectively; the eIF2α-P blot is from its own gel. For (C-E), biological replicates: n = 3. All

1124   error bars represent s.e.m.

1125

1126   **Figure 2**

1127   FRET system monitors eIF2B assembly state. **(A)** Schematic depicting the principle of eIF2B

1128   assembly state modulation by ISRIB and eIF2Bα_2 and FRET readout. **(B-C)** FRET signal

1129   (E_{592}/E_{516}) measured after 1 h of incubation with (B) ISRIB (EC_{50} = 250 nM; s.e.m = 80 nM) or

1130   (C) eIF2Bα_2 (EC_{50} = 20 nM; s.e.m. = 4 nM) at 50 nM eIF2Bβδγε-F. **(D-F)** Timecourse

1131   monitoring FRET signal (E_{592}/E_{516}) after addition of (D) ISRIB (association $t_{1/2}$ = 5.1 min, s.e.m =

1132   0.5 min; dissociation $t_{1/2}$ = 15 min, s.e.m. = 1 min), (E) eIF2Bα_2 (association $t_{1/2}$ = 7.3 min, s.e.m

1133   = 0.6 min; dissociation $t_{1/2}$ = 180 min, s.e.m. = 10 min), or (F) ISRIB + eIF2Bα_2 (association $t_{1/2}$ =

1134   7 min, s.e.m = 1 min; dissociation $t_{1/2}$ = N/A) at 50 nM eIF2Bβδγε-F. At t = 52 min, unlabeled

1135   eIF2Bβδγε was added to a final concentration of 1 μM. For (B-C), representative replicate

1136   averaging four technical replicates are shown. For (D-F), representative replicate averaging

1137   three technical replicates are shown. For (B-F), biological replicates: n = 3. All error bars

1138   represent s.e.m.

1139

1140   **Figure 3**

1141   eIF2B is a decamer in both unstressed and stressed cells, and ISRIB blocks ISR activation. **(A)**

1142   Western blot of K562 ISR reporter cell extracts after treatment with tg or dTag13 for 3 h as

1143   indicated. **(B-D)** FRET signal as monitored by flow cytometry after 3 h treatment with (B)

1144   dTag13 (EC_{50} = 5.1 nM; s.e.m = 0.2 nM), (C) ISRIB +/- 83 nM dTag13 (EC_{50} = 80 nM; s.e.m =

1145   10 nM), (D) various stressors (83 nM dTag13, 50 nM tg, +/- 1.6 μM ISRIB). The ratio of

1146   mScarlet-i / mNeonGreen emission is presented. **(E)** Western blot of K562 ISR reporter cell

1147   extracts treated for 3 h with ISRIB, tg, and/or dTag13 as indicated. All lanes across gels were

1148   loaded with equal total protein. For (A), eIF2Bδ, eIF2Bα, and GAPDH blots, and the ATF4 and

1149   eIF2α blots are from the same gels respectively; the eIF2α-P blot is from its own gel. For (E),

1150   eIF2Bδ, eIF2Bβ, and GAPDH blots, ATF4 and eIF2α blots, and eIF2Bα and eIF2α-P blots are

1151   from the same gels, respectively. For (B-D), biological replicates: n = 3. All error bars represent

1152   s.e.m.

1153

1154   **Figure 4**

1155 ISRIB and eIF2-P compete for eIF2B binding. **(A)** Western blot of K562 ISR reporter cell

1156 extracts after treatment with tg +/- ISRIB as indicated (left panel) or of eIF2B-bound fraction

1157 isolated by anti-FLAG immunoprecipitation of the eIF2B-mNeonGreen-FLAG tagged subunit

1158 under native conditions (right panel). **(B-D)** Plot of fluorescence polarization signal after

1159 incubation of FAM-ISRIB (2.5 nM) with 100 nM eIF2B($\alpha\beta\delta\gamma\epsilon)_2$ and varying concentrations of (B)

1160 ISRIB (IC_{50} = 37 nM; s.e.m. = 1 nM), (C) eIF2 or eIF2-P (IC_{50} = 210 nM; s.e.m. = 120 nM), (D)

1161 eIF2α or eIF2α-P (IC_{50} = 4000 nM; s.e.m. = 200 nM). **(E-F)** Timecourse of fluorescence

1162 polarization signal after addition of (E) eIF2α kinase PKR and ATP or (F) λ phosphatase. FAM-

1163 ISRIB was at 2.5 nM. eIF2B($\alpha\beta\delta\gamma\epsilon)_2$ was at 100 nM. eIF2α and eIF2α-P were at 5.6 μM. In (A),

1164 eIF2Bδ, eIF2Bα, and eIF2α blots, eIF2Bβ and eIF2α-P blots, and ATF4 and GAPDH blots are

1165 from the same gels, respectively. All cell lysate or eIF2B-bound lanes across all gels were

1166 loaded with equal total protein. Biological replicates: (B) n = 3; (C) n = 5 (n = 4 at 2 μM); (D-F) n

1167 =3. All error bars represent s.e.m.

1168

1169 **Figure 5**

1170 eIFα-P is the minimal unit needed to inhibit nucleotide exchange by eIF2B. **(A-D)** GEF activity of

1171 eIF2B as assessed by BODIPY-FL-GDP exchange. eIF2B($\alpha\beta\delta\gamma\epsilon)_2$ was at 10 nM throughout.

1172 For (A) $t_{1/2}$ = 1.6 min (Control), 2.5 min (50 nM eIF2-P), 3.5 min (100 nM eIF2-P), and 7.2 min

1173 (250 nM eIF2-P). For (B) $t_{1/2}$ = 2.4 min (Control), 3.0 min (0.2 μM eIF2α-P), 5.0 min (1 μM

1174 eIF2α-P), and 6.7 min (2 μM eIF2α-P). For (C) $t_{1/2}$ = 1.6 min (Control), 1.9 min (1 μM ISRIB), 3.1

1175 min (250 nM eIF2-P + 1 μM ISRIB), and 7.2 min (250 nM eIF2-P). For (D) $t_{1/2}$ = 1.6 min

1176 (Control), 1.9 min (1 μM ISRIB), 3.1 min (2.5 μM eIF2α-P + 1 μM ISRIB), and 5.3 min (2.5 μM

1177 eIF2α-P). All error bars represent s.e.m. Biological replicates: (A-D) n = 3 except for the 100 and

1178 50 nM eIF2-P conditions in (A) where n = 2.

1179

1180 **Figure 6**

1181 eIFα-P reduces eIF2B's catalytic activity and antagonizes eIF2 binding. **(A)** Initial velocity of

1182 eIF2B-catalyzed nucleotide exchange as a function of eIF2 concentration. eIF2B($\alpha\beta\delta\gamma\epsilon)_2$

1183 concentration was 10 nM. **(B)** Plot of k_{cat} / K_M for tetramer and decamer at varying eIF2α-P

1184 concentrations, obtained by fitting the linear portion of the Michaelis Menten saturation curve.

1185 Keeping the number of eIF2 binding sites constant, the eIF2B($\alpha\beta\delta\gamma\epsilon)_2$ concentration was 10 nM

1186 while eIF2B$\beta\delta\gamma\epsilon$ was 20 nM. **(C)** Western blot of purified protein recovered after incubation with

1187 eIF2B($\alpha\beta\delta\gamma\epsilon)_2$ immobilized on Anti-protein C antibody conjugated resin. eIF2Bα was protein C

1188 tagged. **(D)** Plot of fluorescence polarization signal before (*black*) and after incubation of FAM-

1189   ISRIB (2.5 nM) with 100 nM eIF2B(αβδγε)$_2$ (*red*) or 100 nM eIF2B(αβδγε)$_2$ + 6.0 μM eIF2α-P

1190   and varying concentrations of eIF2 (*blue*). For elution samples In (C), eIF2β, eIF2Bε, and

1191   eIF2Bα, and the eIF2Bδ and eIF2α-P blots are from the same gels, respectively. For input

1192   samples eIF2β and eIF2Bα, and the eIF2Bδ and eIF2α-P blots are from the same gels,

1193   respectively; eIF2Bε is from its own gel. Biological replicates: (A-B) n = 2; (D) n = 3. All error

1194   bars represent s.e.m.

1195

1196   **Figure 7**

1197   eIF2α-P binding conformationally inactivates eIF2B. **(A)** Overlay of the ISRIB-bound eIF2B

1198   structure (PDB ID: 6CAJ) to the eIF2α-P-bound eIF2B structure (PDB ID: 6O9Z). The 7.5

1199   degree hinge movement between the two eIF2B halves was measured between the lines

1200   connecting eIF2Bε H352 and P439 in the ISRIB-bound vs. eIF2α-P-bound structures. **(B)** Zoom-

1201   in view of the ISRIB binding pocket upon eIF2α-P binding. The ~2 Å pocket lengthening was

1202   measured between eIF2Bδ and eIF2Bδ' L482; the "prime" to indicate the subunit of the

1203   opposing tetramer. ISRIB is shown in stick representation. **(C)** Overlay of eIF2-bound eIF2B

1204   (PDB ID: 6O85) and eIF2α-P-bound eIF2B. The 2.6 Å widening of the eIF2 binding site induced

1205   by eIF2α-P binding was measured between E139 and R250 of eIF2Bβ and eIF2Bδ',

1206   respectively. The side chains involved in the key cation-π interaction between R250 in eIF2Bδ

1207   and Y81 in eIF2α that is lost due to pocket expansion are shown **(D)** Overlay of the eIF2-bound

1208   eIF2B to the eIF2α-P-bound eIF2B. The 5.5 Å narrowing of the eIF2α-P binding pocket causing

1209   a steric clash between eIF2Bα and eIF2α-P in the eIF2-bound state was measured between

1210   eIF2Bα S77 and eIF2Bδ L314. ISRIB-bound eIF2B is colored in *gold*, eIF2α-P-bound eIF2B in

1211   *blue* and eIF2-bound eIF2B in *light green*. eIF2α-P is shown in *pink* and eIF2α in *red*. ISRIB is

1212   colored In *CPK*.

1213

1214   **Figure 8**

1215   Model for modulation of eIF2B activity. ISRIB and eIF2 binding to eIF2B stabilize the active,

1216   "wings up" conformation of eIF2B (A-State) while both eIF2-P (as well as eIF2α-P alone; not

1217   shown) stabilize the inactive "wings down" conformation of eIF2B (I-State), which cannot

1218   engage ISRIB and exhibits reduced enzymatic activity and eIF2 binding (akin to an eIF2Bβδγε

1219   tetramer). As indicated by the structure of the apo eIF2B decamer, the conformational

1220   equilibrium in the absence of ligand likely favors the A-State, which is further stabilized by

1221   substrate eIF2 and/or ISRIB binding but antagonized by eIF2-P binding.

1222

1223 **Table 1.** Data collection, reconstruction, and model refinement statistics for the apo eIF2B

1224 decamer.

1225

1226 **Table 2.** Data collection, reconstruction and refinement statistics for the ISRIB-bound eIF2B

1227 decamer.

1228
1229 **Table 3.** Antibodies for Western Blotting.

1230

1231 **Table 4.** Oligos and sgRNAs.

1232

1233

Supplemental Information

Figure 1-figure supplement 1

Overview of key eIF2 and eIF2B interaction surfaces. A surface representation of a model of two eIF2 heterotrimers and ISRIB bound to an eIF2B decamer is shown (PDB ID: 6O85). Individual subunits of eIF2 and eIF2B are indicated. The eIF2 heterotrimers are outlined in white and the locations of interfaces IF1 - IF4 are indicated, as are the positions of eIF2α S51, the GTP binding pocket (empty in the structure), and ISRIB (shown in stick representation). The eIF2Bα$_2$ dimer is hidden in this orientation. eIF2Bε contains two domains linked by a flexible tether which was not resolved in the structure.

Figure 1-figure supplement 2

Tagging of eIF2B subunits in K562 cells. **(A)** Western blot of eIF2B subunits in parental and edited K562 cells. ISR Reporter cells and Assembly State Reporter cells were edited at the *EIF2B1* locus (eIF2Bα-FKBP12^{F36V} N-terminal fusion). No evidence of WT protein is observed in either cell line. Assembly State Reporter cells were edited at the *EIF2B2* locus (eIF2Bβ-mNeonGreen C-terminal fusion) and the *EIF2B4* locus (eIF2Bδ-mScarlet-i C-terminal fusion). No evidence of WT protein is observed in these cells. The asterisk denotes a non-specific band. The double asterisk denotes a minor eIF2Bδ species likely resulting from mScarlet-i / G/S linker proteolysis during sample preparation. eIF2Bδ and eIF2Bα blots and eIF2Bε and GAPDH blots are from the same gel, respectively; eIF2Bβ is from its own blot. **(B)** 1% agarose gel of PCR amplified eIF2Bα-, eIF2Bβ-, and eIF2Bδ-encoding loci from parental and edited cell line gDNA preps. The lengths of the eIF2Bβ and eIF2Bδ products demonstrate that no unedited alleles are present in the Assembly State reporter cells. The length of the eIF2Bα product demonstrates that some tagged as well as some untagged alleles are present in both cell lines. Based on the lack of WT length protein the remaining untagged alleles likely harbor deletions or frameshift mutations that prevent synthesis or destroy the protein product. The asterisk denotes a non-specific band.

Figure 1-figure supplement 3

ISR reporter design. A schematic of the ATF4 Translation and General Translation reporters used to read out ISR activation.

Figure 1-figure supplement 4

1268   Decreases in general translation after eIF2Bα depletion. **(A-C)** General translation reporter

1269   signal from the experiments shown in (A) Figure 1C, (B) Figure 1D, and (C) Figure 1E.

1270

1271   **Figure 1-figure supplement 5**

1272   dTag13 treatment alone does not activate the ISR. Parental cells containing the ATF4 and

1273   general translation reporters as well as the edited cells where eIF2Bα was tagged with an

1274   FKBP12^{F36V} degron were treated with 500 nM dTag13 or untreated (0.1% DMSO) for 24 h and

1275   then 20 μM trimethoprim for 3 h. ATF4 and General translation reporter levels were monitored

1276   by flow cytometry and the change in reporter signal between dTag13 treated and untreated

1277   conditions is shown. dTag13 only activates the ISR when eIF2Bα is endogenously tagged with

1278   the FKBP12^{F36V} degron.

1279

1280   **Figure 2-figure supplement 1**

1281   eIF2Bβδγε-F can octamerize and decamerize. Analytical ultracentrifugation (sedimentation

1282   velocity) was used to determine eIF2B complex assembly state. Treatment with ISRIB induces

1283   octamerization of eIF2Bβδγε-F. Treatment with eIF2Bα$_2$ induces decamerization. 1 μM ISRIB, 1

1284   μM eIF2Bβδγε-F, and 500 nM eIF2Bα$_2$ were used.

1285

1286   **Figure 2-figure supplement 2**

1287   Validation of eIF2Bβδγε-F kinetics. **(A-C)** Treatment of 50 nM eIF2Bβδγε-F with ISRIB or

1288   eIF2Bα$_2$ led to no changes in FRET signal when simultaneously treated with excess of

1289   untagged eIF2Bβδγε (1 μM).For (A-C), representative replicate averaging three technical

1290   replicates are shown. Biological replicates: n = 2. All error bars represent s.e.m.

1291

1292   **Figure 2-figure supplement 3**

1293   ISRIB treatment does not impact GEF activity when eIF2Bα$_2$ is saturating. GEF activity of eIF2B

1294   as assessed by BODIPY-FL-GDP exchange. BODIPY-FL-GDP fluorescence decreases when

1295   free in solution. $t_{1/2}$ = 1.6 min (Control) and 1.9 min (1 μM ISRIB). Biological replicates: n = 3.

1296

1297   **Figure 6-figure supplement 1**

1298   eIF2α-P decreases the initial velocity of eIF2B's GEF activity. **(A-E)** Initial velocity of the eIF2B

1299   GEF reaction under varying conditions. Initial velocity was determined by a linear fit to

1300   timepoints acquired from 50 – 200 seconds (panels A - C) or 400 - 1000 seconds (panels D - E)

1301   after addition of eIF2B. For panels A – E, representative replicates of n = 2 biological replicates

1302   are shown.

1303

1304   **Figure 7-figure supplement 1**

1305   Cryo-EM workflow for apo-eIF2B decamer. **(A)** Representative micrograph showing the quality

1306   of data used for the final reconstruction of the apo eIF2B structure. **(B)** Data processing scheme

1307   of the apo eIF2B. **(C)** Fourier Shell Correlation (FSC) plots of the 3D reconstructions of the apo

1308   eIF2B masked (dark blue), unmasked (orange) and map to model (yellow). **(D)** Orientation

1309   angle distribution of the apo eIF2B reconstruction. **(E)** Local resolution map of the apo eIF2B

1310   showing that the peripheral regions of the gamma and alpha subunits are dynamic. (**F**) EM

1311   maps of different regions of the apo eIF2B structure showing the quality of the data and the fit of

1312   the model. Regions close to the core (chain D, on the left) are well-resolved and have clear

1313   density for most side chains; regions close to the periphery of the molecule (chains A and I,

1314   middle and right) are less well-resolved due to higher flexibility.

1315

1316   **Figure 7-figure supplement 2**

1317   ISRIB binding induces local pocket changes. **(A)** Overlay of ISRIB-bound eIF2B (PDB ID: 6CAJ)

1318   to the apo eIF2B (PDB ID: 7L70) showing both structures share a similar global conformation.

1319   **(B)** Zoom-in view of the ISRIB-binding pocket showing that in the apo state L179 occupies a

1320   position in the ISRIB-binding pocket that would clash with ISRIB binding. H188 changes its

1321   rotameric conformation upon ISRIB binding. The apo eIF2B is shown in *green*, and the ISRIB-

1322   bound eIF2B in *gold*. ISRIB is shown in stick representation, colored in *CPK*.

1323

1324   **Figure 7-figure supplement 3**

1325   eIF2-P binding pulls IF4 away but leaves IF1 - IF3. Overlay of eIF2-bound eIF2B (PDB ID:

1326   6O85) and eIF2α-P-bound eIF2B (PDB ID: 6O9Z). IF4 is pulled away from IF3 by 2.6 Å but IF1

1327   (eIF2Bε Catalytic and eIF2γ), IF2 (eIF2Bε Core and eIF2γ), and IF3 (eIF2Bβ and eIF2α) remain

1328   available for eIF2 binding. eIF2α-P-bound eIF2B in *blue* and eIF2-bound eIF2B in *light green*.

1329   eIF2γ is shown in *purple*, eIF2β in *pink,* and eIF2α in *red*. ISRIB is colored in *CPK*.

1330

1331   **Figure 7-figure supplement 4**

1332   Re-refinement of the ISRIB-bound eIF2B decamer. **(A)** The distal portion of the original model

1333   eIF2Bα from the ISRIB-bound eIF2B decamer placed within EMDB:7443 after lowpass filtering

1334   to 3.0Å resolution. There is a helix (amino acids 44-56) out of place. The average CC value for

1335 the chains belonging to eIF2Bα from this model is ~0.74. **(B)** After manual adjustments in Coot
1336 and re-refinement in phenix.real_space_refine, this short helix is placed inside the cryo-EM
1337 density with an average CC value for the chains belonging to eIF2Bα of ~0.77. **(C)** The map-to-
1338 model Fourier Shell Correlation plots of the updated model.
1339
1340 **EM Validation Report.**
1341
1342
1343
1344
1345
1346
1347
1348
1349
1350
1351
1352
1353
1354
1355
1356
1357
1358
1359
1360
1361
1362
1363
1364
1365
1366
1367
1368

1369 **Table 1.** *Data collection, reconstruction, and model refinement statistics for the apo eIF2B*
1370 *decamer*
1371
1372

Structure	Apo eIF2B decamer (PDB ID: 7L70; EMD-23209)
Data collection	
Microscope	Titan Krios
Voltage (keV)	300
Nominal magnification	105000x
Exposure navigation	Image shift
Electron dose (e$^-$Å^{-2})	67
Dose rate (e$^-$/pixel/sec)	8
Detector	K3 summit
Pixel size (Å)	0.835
Defocus range (μm)	0.6-2.0
Micrographs	1699
Reconstruction	
Total extracted particles (no.)	461805
Final particles (no.)	198362
Symmetry imposed	C1
FSC average resolution, masked (Å)	3.8
FSC average resolution, unmasked (Å)	2.8
Applied B-factor (Å)	92.4
Reconstruction package	Cryosparc 2.15
Refinement	
Protein residues	3156
Ligands	0
RMSD Bond lengths (Å)	0.004
RMSD Bond angles ($^{\circ}$)	0.978
Ramachandran outliers (%)	0.06
Ramachandran allowed (%)	3.81
Ramachandran favored (%)	96.13
Poor rotamers (%)	2.61
CaBLAM outliers (%)	2.00
Molprobity score	1.83
Clash score (all atoms)	4.77
B-factors (protein)	88.43
B-factors (ligands)	N/A
EMRinger Score	2.68
Refinement package	Phenix 1.17.1-3660-000

1373
1374
1375
1376
1377
1378
1379
1380
1381
1382
1383
1384
1385
1386
1387
1388
1389
1390
1391
1392
1393
1394
1395
1396
1397
1398
1399
1400
1401
1402
1403
1404
1405
1406
1407
1408
1409
1410
1411
1412
1413
1414

1415
1416
1417
1418

1419 **Table 2.** *Data collection, reconstruction and refinement statistics for the ISRIB-bound eIF2B*
1420 *decamer*

Structure	ISRIB-bound eIF2B decamer from Janelia (PDB ID: 6CAJ) (Tsai et al. 2018)	ISRIB-bound eIF2B decamer from Berkeley (PDB ID: 6CAJ) (Tsai et al. 2018)
Data collection		
Voltage (keV)	300	300
Nominal magnification	29000x	29000x

1421
1422

Per frame electron dose (e⁻Å⁻²)	1.19	1.63
Spherical aberration (mm)	2.7	2.62
# of frames	67	27
Detector	K2 summit	K2 summit
Pixel size (Å)	1.02	0.838
Defocus range (μm)	-0.3 to -3.9	-0.3 to -3.9
Micrographs	1780	1515
Frame length (s)	0.15	0.18
Detector pixel size (μm)	5.0	5.0

Reconstruction Using Particles From Both Datasets After Magnification Rescaling

Particles following 2D classification	202,125
FSC average resolution unmasked (Å)	3.4
FSC average resolution masked (Å)	3.0
Map sharpening B-factor	-60

Refinement

PDB ID: 7L7G (Update to 6CAJ); EMD-7443

Protein residues	3198
Ligands	1
RMSD Bond lengths (Å)	0.004
RMSD Bond angles (°)	0.967
Ramachandran outliers (%)	0.00
Ramachandran allowed (%)	5.40
Ramachandran favored (%)	94.60
Poor rotamers (%)	1.00
Molprobity score	1.81
Clash score (all atoms)	7.95
B-factors (protein)	65.93
B-factors (ligands)	52.57
EMRinger Score	2.37
Refinement package	Phenix 1.17.1-3660-000

1423

1424

1425

1426

1427

1428

1429

1430 **Table 3.** Antibodies for Western Blotting.

1431

Antibody Target	Host	Dilution	Manufacturer	Blocking Conditions
GAPDH	rabbit	1/2000	Abcam	TBS-T + 3% BSA
eIF2Bα	rabbit	1/1000	ProteinTech	TBS-T + 3% milk
eIF2Bβ	rabbit	1/1000	ProteinTech	TBS-T + 3% milk
eIF2Bδ	rabbit	1/1000	ProteinTech	TBS-T + 3% milk
eIF2Bε	mouse	1/1000	Santa Cruz Biotechnology	PBS-T + 3% milk
ATF4	rabbit	1/1000	Cell Signaling	PBS-T + 3% milk

eIF2α-P	rabbit	1/1000	Cell Signaling	PBS-T + 1% BSA
eIF2α	rabbit	1/1000	Cell Signaling	PBS-T + 3% milk
eIF2β	rabbit	1/1000	ProteinTech	PBS-T + 3% milk
eIF2γ	rabbit	1/500	ProteinTech	PBS-T + 3% milk

1432
1433
1434
1435
1436
1437   **Table 4.** Oligos and sgRNAs.

1438

Oligo	Sequence	Use
oMS266	/5InvddT/G*G*G*A*A*CCTCTTCTGTAACTCCTTAGC	Amplify HDR template
oMS267	/5InvddT/C*C*T*G*A*G*GGCAAACAAGTGAGCAGG	Amplify HDR template
oMS269	TCGTGCCAGCCCCCTAATCT	Validate eIF2Bα tagging
oMS270	CTGAACGGCGCTGCTGTAGC	Validate eIF2Bα tagging
oMS256	AGTGAACTCTACCATCCTGA	Validate eIF2Bβ tagging
oMS258	TTAGGTGGACTCCTGTGC	Validate eIF2Bβ tagging
oMS096	CTGGCTAACTGGCAGAACC	Validate eIF2Bδ tagging
oMS268	AGAAACAAAGGCAGCAGAGT	Validate eIF2Bδ tagging
sgMS001	CAATCTGCTTAGGACACGTG	Target Cas9 to eIF2Bβ C-terminus
sgMS004	AGAGCAGTGACCAGTGACGG	Target Cas9 to eIF2Bδ C-terminus
sgMS006	GTGTGTGGTTGTCATTAGGG	Target Cas9 to eIF2$\alpha\beta$ N-terminus

1439

1440
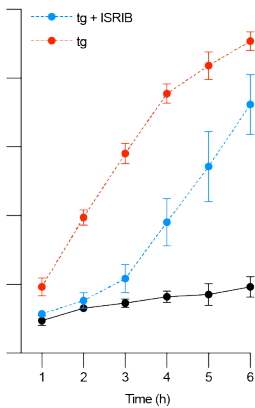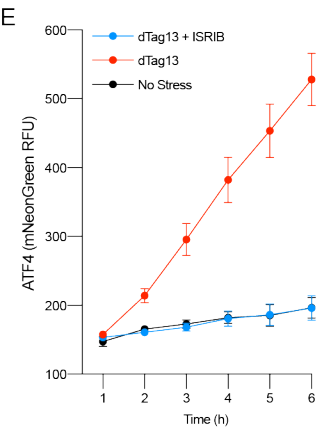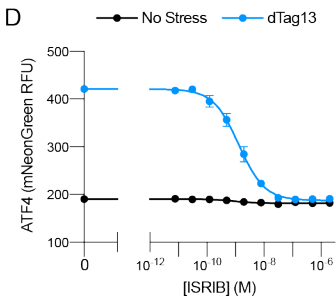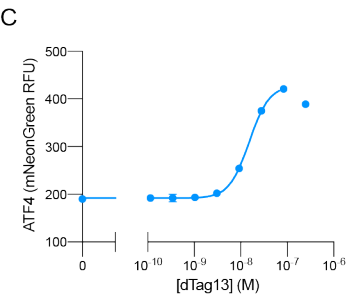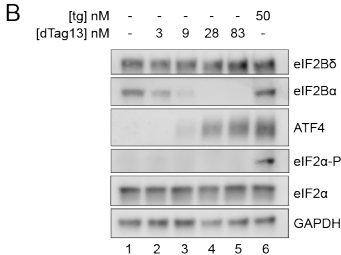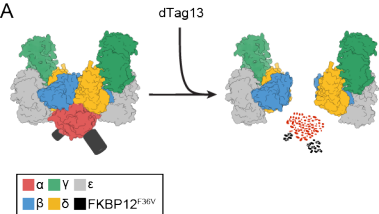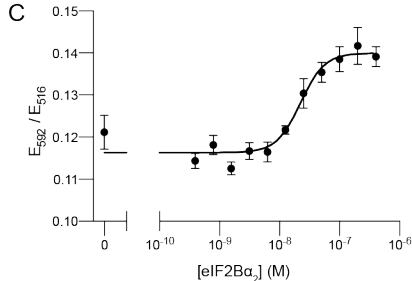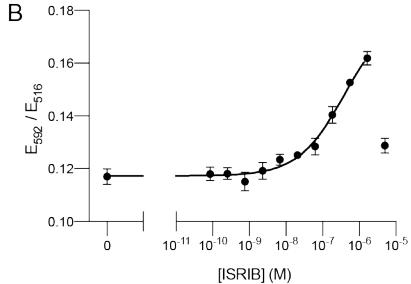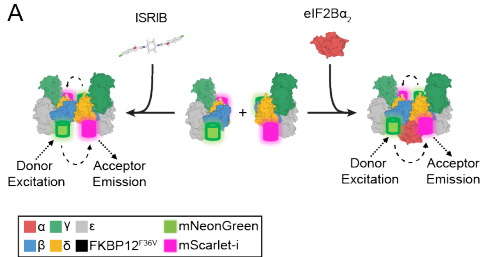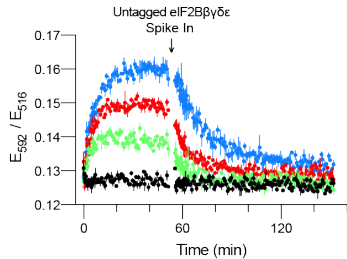
A — ISRIB, eIF2Bα₂

Donor Excitation, Acceptor Emission

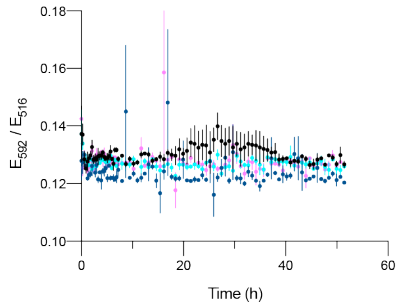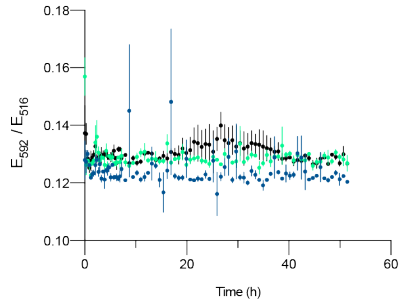α γ ε mNeonGreen
β δ FKBP12^{F36V} mScarlet-i

B

C
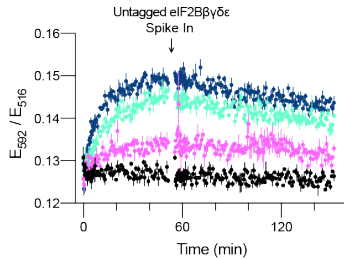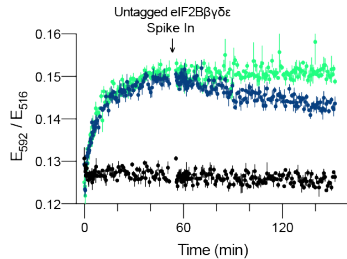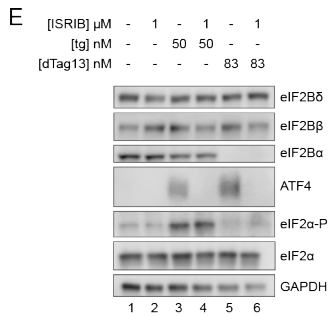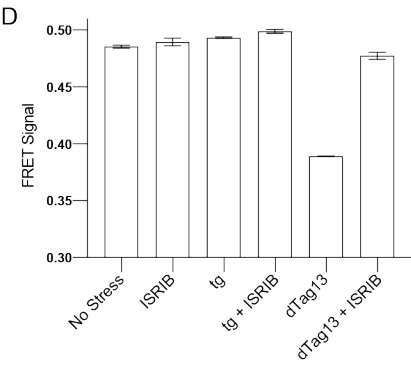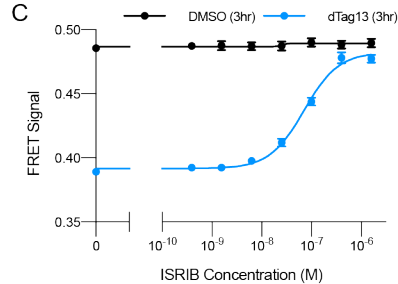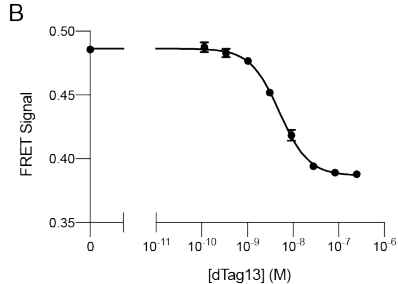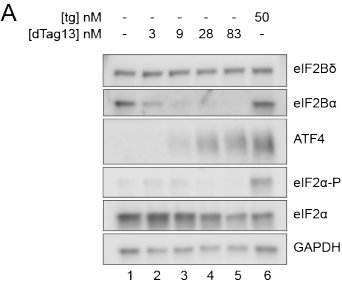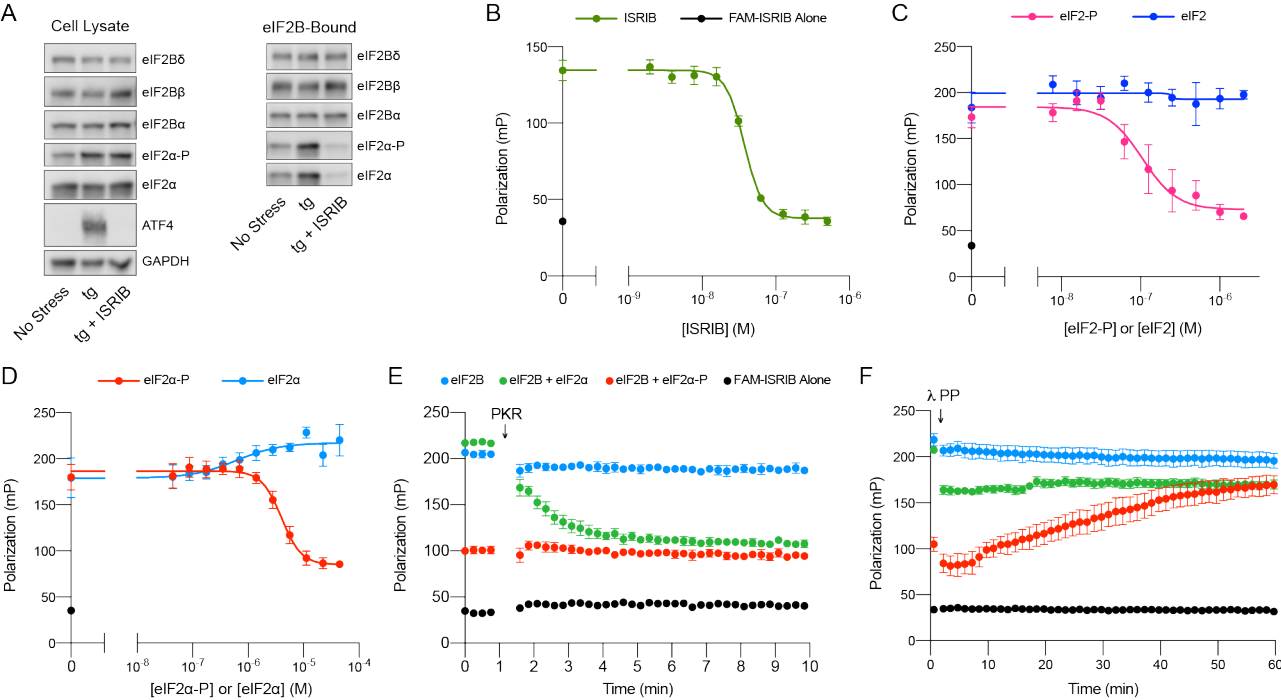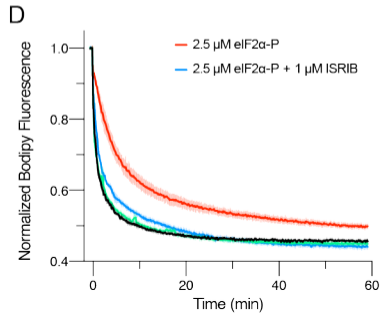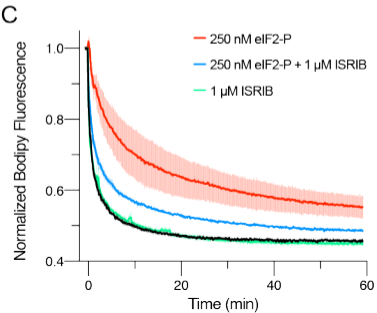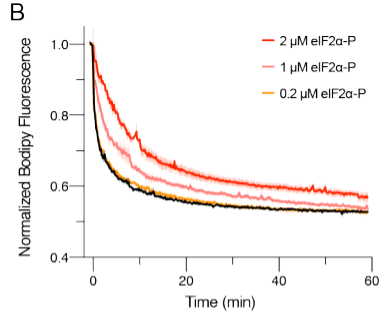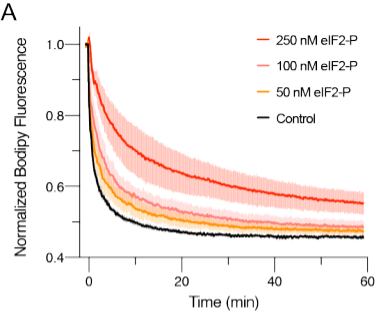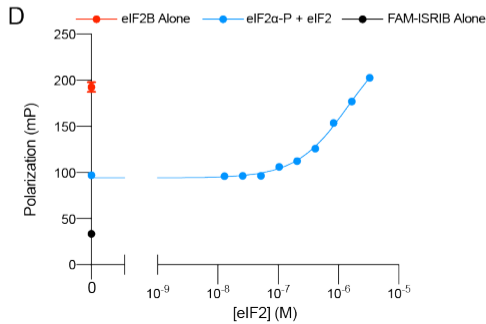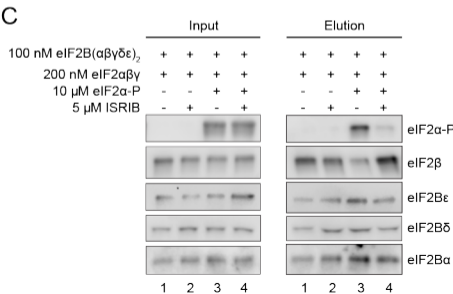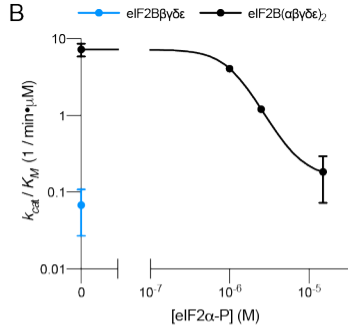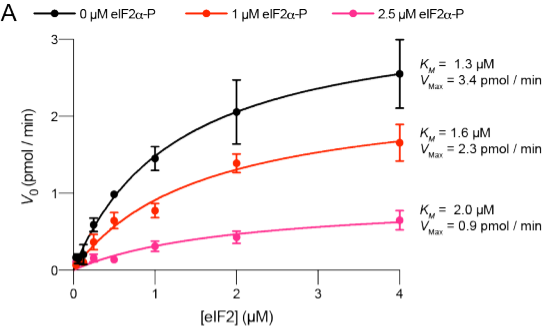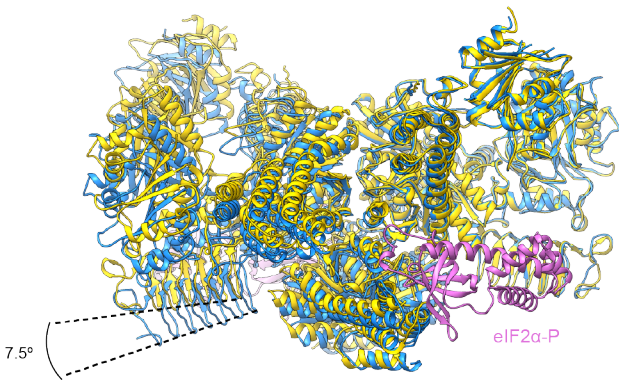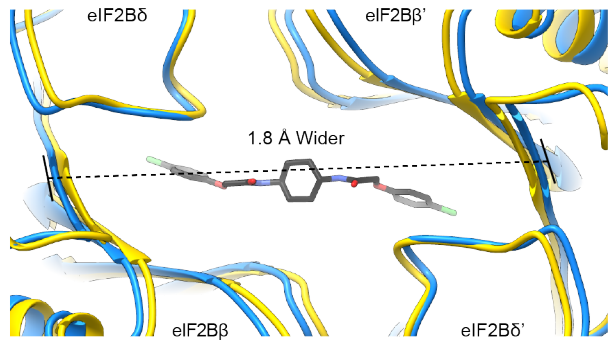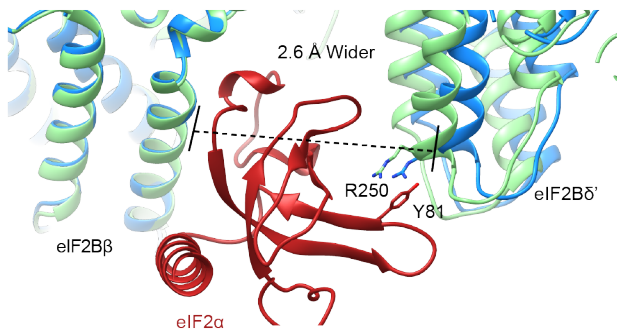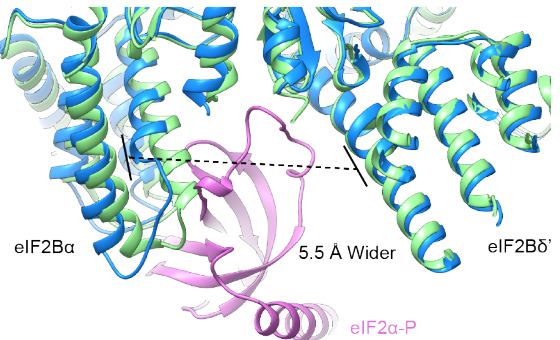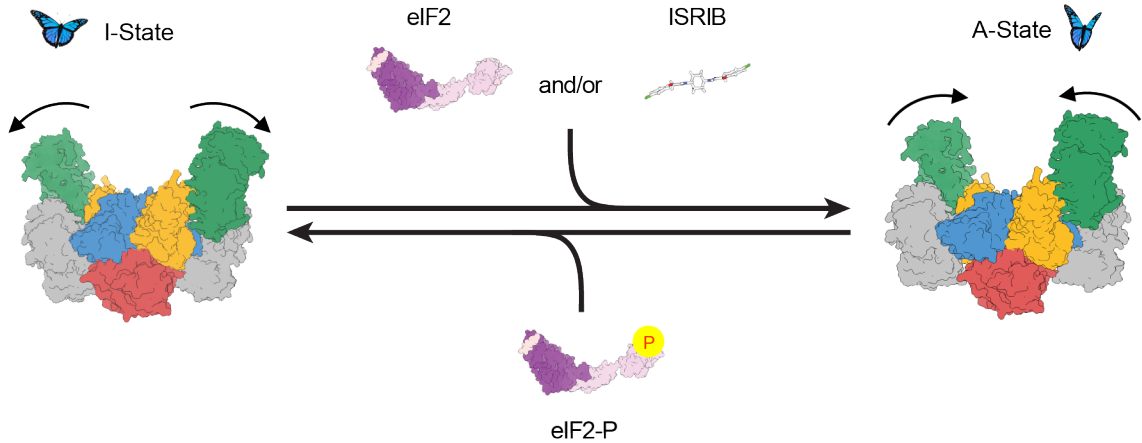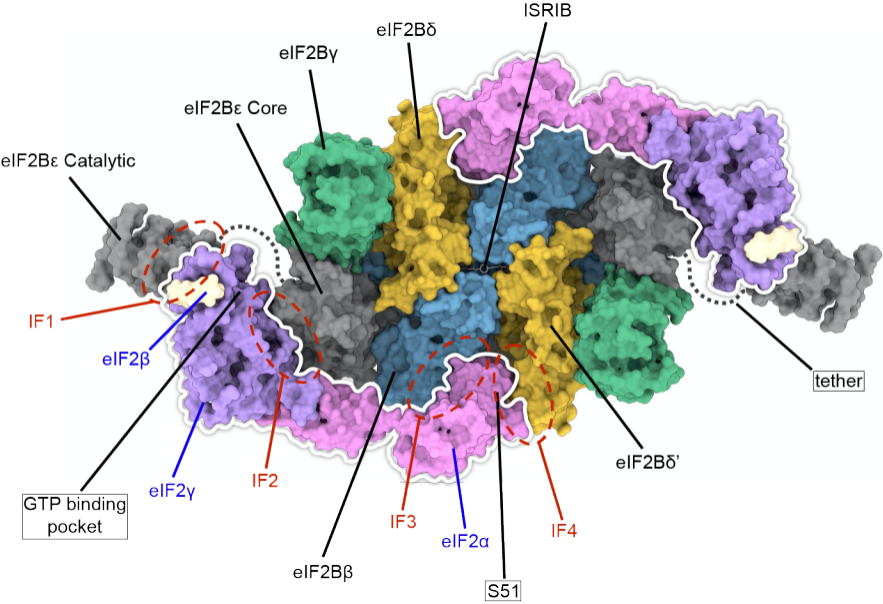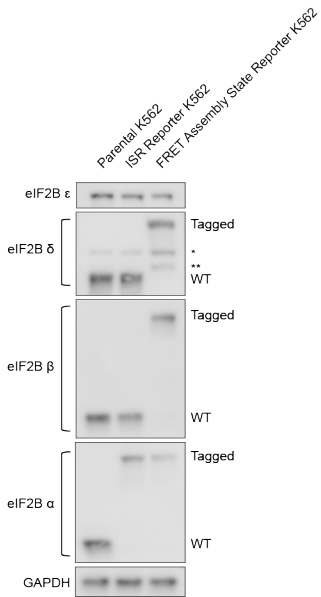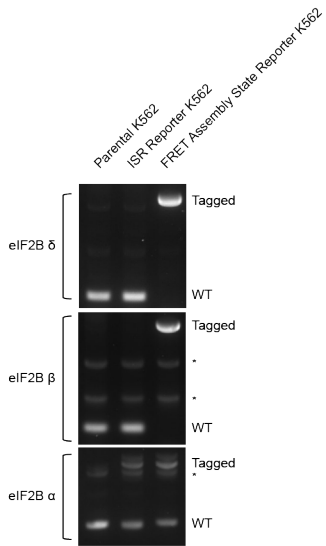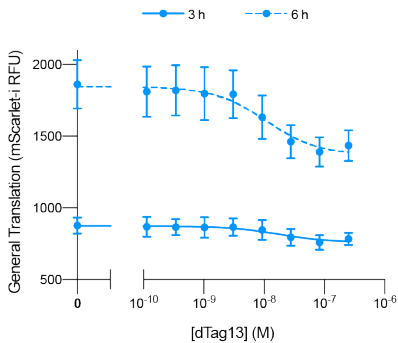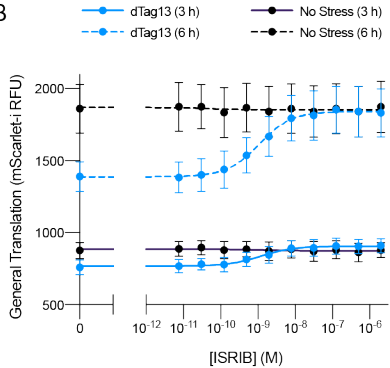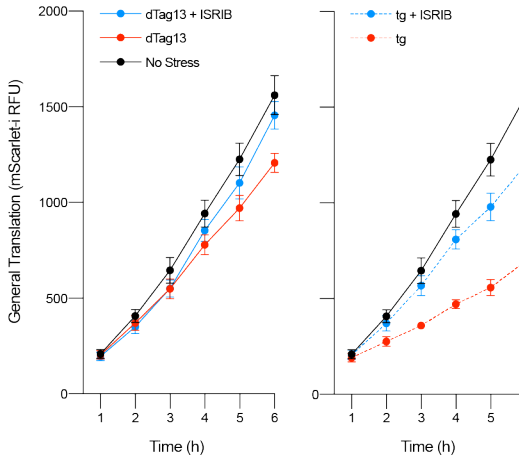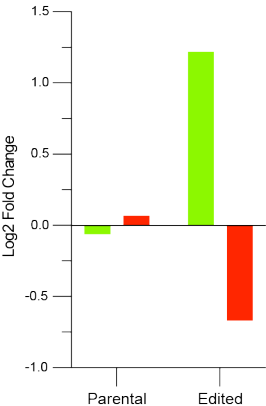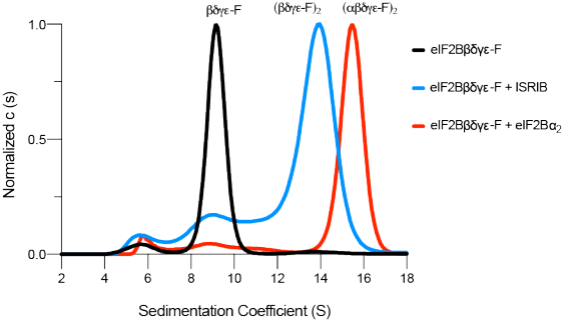
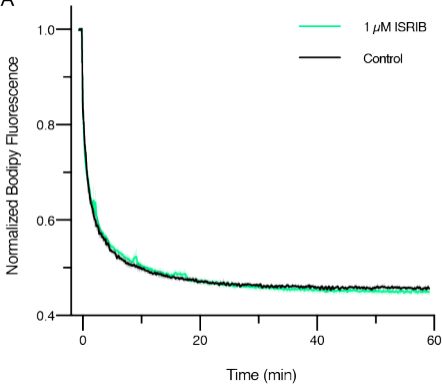**D** • Buffer • 167 nM ISRIB • 500 nM ISRIB • 1500 nM ISRIB

E • 12.5 nM eIF2Bα₂ • 50 nM eIF2Bα₂ • 200 nM eIF2Bα₂
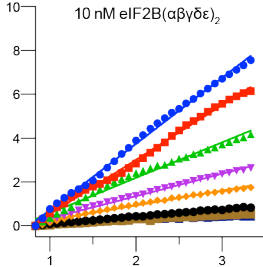
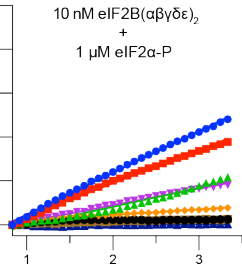**F** • 200 nM eIF2Bα₂ • 200 nM eIF2Bα₂ + 1500 nM ISRIB

A

● 0 μM eIF2α-P	● 1 μM eIF2α-P	● 2.5 μM eIF2α-P

K_M = 1.3 μM
V_{Max} = 3.4 pmol / min

K_M = 1.6 μM
V_{Max} = 2.3 pmol / min

K_M = 2.0 μM
V_{Max} = 0.9 pmol / min

V_0 (pmol / min)

[eIF2] (μM)

B

● eIF2Bβγδε   ● eIF2B(αβγδε)$_2$

k_{cat} / K_M (1 / min•μM)

[eIF2α-P] (M)

C

	Input	Elution
100 nM eIF2B(αβγδε)$_2$	+ + + +	+ + + +
200 nM eIF2αβγ	+ + + +	+ + + +
10 μM eIF2α-P	- - + +	- - + +
5 μM ISRIB	- + - +	- + - +

eIF2α-P
eIF2β
eIF2Bε
eIF2Bδ
eIF2Bα

1 2 3 4   1 2 3 4

D

● eIF2B Alone   ● eIF2α-P + eIF2   ● FAM-ISRIB Alone

Polarization (mP)

[eIF2] (M)

A ISRIB-bound eIF2B   eIF2α-P-bound eIF2B

7.5°

eIF2α-P

B eIF2Bδ   eIF2Bβ'

1.8 Å Wider

eIF2Bβ   eIF2Bδ'

C eIF2-bound eIF2B   eIF2α-P-bound eIF2B

2.6 Å Wider

R250
Y81

eIF2Bβ   eIF2Bδ'

eIF2α

D eIF2Bα   eIF2Bδ'

5.5 Å Wider

eIF2α-P

I-State

eIF2

ISRIB

and/or

A-State

eIF2-P

A

B

ATF4 Reporter

uORF 1   uORF 2

Full ATF4 5' UTR | ATF4 - first 28 amino acids | ecDHFR degron | mNeonGreen

General Translation Reporter

Partial ATF4 5' UTR | ecDHFR degron | mScarlet-i

A

A, B, C, D, E panels: plots of eIF2 loaded with BODIPY-FL-GDP (pmol) versus Time (min).

A: 10 nM eIF2B(αβγδε)₂

B: 10 nM eIF2B(αβγδε)₂ + 1 μM eIF2α-P

C: 10 nM eIF2B(αβγδε)₂ + 2.5 μM eIF2α-P

D: 10 nM eIF2B(αβγδε)₂ + 15 μM eIF2α-P

E: 20 nM eIF2Bβγδε

[eIF2]
- 4 μM
- 2 μM
- 1 μM
- 500 nM
- 250 nM
- 125 nM
- 62.5 nM
- 31.75 nM
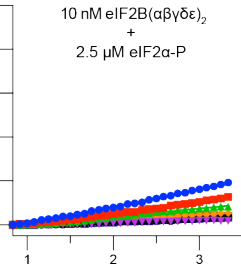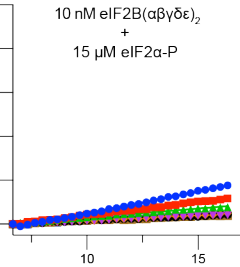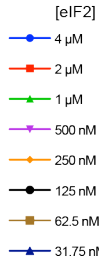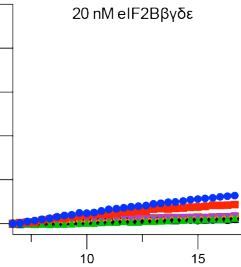
A
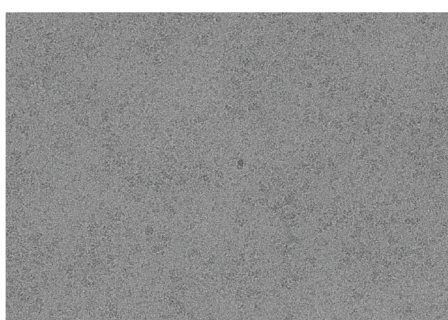
B

461805 particles, 2D classifications (0.835 Å) in Cryosparc
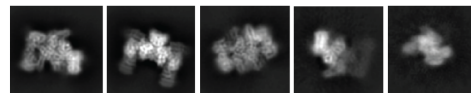
426271 particles

Heterogenous refinement in Cryosparc using EMDB 7442 as starting models
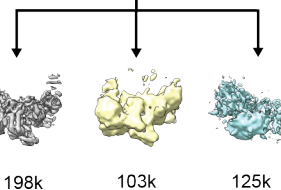
198k   103k   125k

Homogeneous refinement
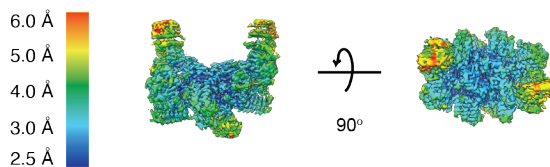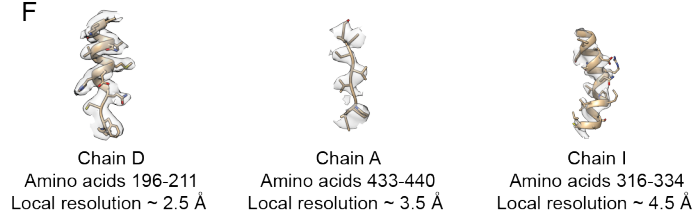
2.9 Å

Nonuniform refinement

2.8 Å

C

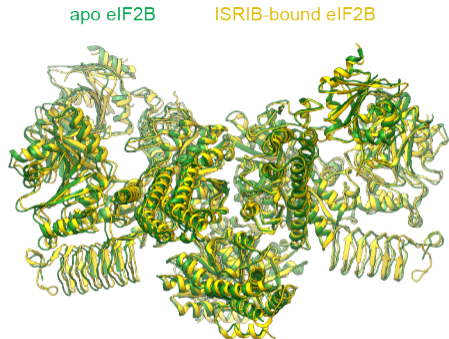FSC (masked)
FSC (unmasked)
FSC (map to model, unmasked)
FSC (map to model, masked)

3.8 Å   2.8 Å

0.143

Spatial Frequency 1/Å

D

# of images

Azimuth

E

6.0 Å
5.0 Å
4.0 Å
3.0 Å
2.5 Å

90°

F

Chain D
Amino acids 196-211
Local resolution ~ 2.5 Å

Chain A
Amino acids 433-440
Local resolution ~ 3.5 Å

Chain I
Amino acids 316-334
Local resolution ~ 4.5 Å

eIF2-bound eIF2B   eIF2α-P-bound eIF2B

eIF2Bε Core

eIF2Bε Catalytic

IF1

IF2

eIF2β

eIF2Bβ

IF3

IF4

eIF2Bδ'

eIF2γ

eIF2α

A

B

C

FSC (map to model, unmasked)

FSC (map to model, masked)

0.5

3.5 Å   3.2 Å

3.1 Å   3.0 Å

0.143